Microtubule pivoting driven by spindle elongation rescues polar chromosomes to ensure faithful mitosis

Isabella Koprivec*[1], Valentina Štimac*[1], Petra Mikec[1], Iva M. Tolić[#1]

* These authors contributed equally to this work
[#] Corresponding author

[1] Ruđer Bošković Institute, Bijenička cesta 54, 10 000 Zagreb, Croatia

Abstract

Polar chromosomes represent a subset of ~7 chromosomes in human cells that first attach to the mitotic spindle behind the spindle pole. These chromosomes are delayed in congression to the metaphase plate and prone to segregation errors. Yet, their mechanism of congression remains elusive. By using stimulated emission depletion (STED) and lattice light-sheet (LLS) microscopy, here we show that polar chromosomes require a unique congression step to transit across the spindle pole. This step occurs independently of the known congression drivers, including CENP-E, kinetochore dynein, chromokinesins, and actomyosin. Instead, it relies on the pivoting of chromosome-carrying astral microtubules around the centrosome towards the spindle surface. During pivoting, polar chromosomes form complex attachments with astral microtubules that persist throughout the process. By altering the kinesin-5 Eg5/KIF11 activity to reverse, restore, or block spindle elongation, we show that spindle elongation drives the pivoting and dictates its direction and magnitude. We reveal impaired spindle elongation as a major cause of congression defects and segregation errors of polar chromosomes in RPE1 cells after Mps1 kinase inhibition, and in the high-grade serous ovarian carcinoma OVSAHO cells. Increasing spindle elongation efficiency by depleting the kinesin-4 KIF4A rescued polar chromosomes in OVSAHO cells, supporting the causal relationship between spindle elongation and resolution of polar chromosomes. We conclude that polar chromosomes depend on spindle elongation to propel the pivoting of their astral microtubules, enabling their contact with the spindle surface, congression, and proper segregation. In the context of disease, our findings suggest that altering spindle elongation has the potential to modify mitotic errors in certain cancer cells.

Introduction

Chromosomes must efficiently congress to the equatorial plane to ensure mitotic fidelity (Maiato et al., 2017). Based on their position at the nuclear envelope breakdown (NEBD), chromosomes undertake different pathways toward the equator, resulting in distinct congression efficiencies and segregation error rates (Vukušić and Tolić, 2022). Chromosomes behind the spindle poles are particularly problematic, as they are shielded by the pole and require a multi-step process to reach the equator (Barisic et al., 2014; Klaasen et al., 2022). After approaching the spindle pole from the back using the joint activity of kinetochore dynein and nuclear actomyosin (Barisic et al., 2014; Booth et al., 2019; Li et al., 2007; Rieder and Alexander, 1990; Yang et al., 2007), these chromosomes later on travel along the main spindle surface using the joint activity of CENP-E at kinetochores, pulling forces by end-on attached microtubules, and polar ejection forces (Barisic et al., 2014; Cai et al., 2009; Craske and Welburn, 2020; Kapoor et al., 2006; McEwen et al., 2001; Renda et al., 2022; Shrestha and Draviam, 2013; Vukušić and Tolić, 2023; Wandke et al., 2012). Yet none of these steps explain how they cross the pole and switch sides from the back to the front of the spindle.

Chromosomes that fail to escape the area behind the pole before the spindle fully forms risk stabilization of improper attachments, ER ensheathment, and missegregation in case of the spindle assembly checkpoint (SAC) weakness, bypass or delayed satisfaction (Dick and Gerlich, 2013; Ferrandiz et al., 2022; Gomes et al., 2022; Kabeche and Compton, 2013; Klaasen et al., 2022). Recent studies discovered that such unaligned (i.e. behind the spindle pole) and misaligned (i.e. near the pole within the main spindle surface) chromosomes represent an important source of segregation errors, with the highest probability of ending up in micronuclei, the strongest correlation with chromosomal instability, and a direct link to metastatic potential (Gomes et al., 2022; Tucker et al., 2023). Several labs have now observed mis- and unaligned chromosomes in cancer cell lines, such as ovarian, bone, colorectal and breast cancer, and in patient samples of primary and metastatic breast cancer (Ertych et al., 2014; Gomes et al., 2022; Tamura et al., 2020; Tucker et al., 2023). Mupltiple lines of evidence also indirectly suggest that chromosome 1, whose 1q arm gain directly leads to cancer development and malignant transformation, might often be located behind the pole and thus at risk from unalignment (Bolzer et al., 2005; Girish et al., 2023; Klaasen et al., 2022; Tovini and McClelland, 2019). While this implication further highlights the importance of escaping the polar region on time, the reason why chromosomes occasionally fail to do so remains elusive.

Here, we apply a unique synergy of stimulated emission depletion (STED), lattice light-sheet (LLS) and confocal microscopy, combined with molecular perturbations, to overcome optical and spatiotemporal resolution barriers that prevented studies of polar chromosome dynamics, which occurs quickly during early prometaphase within a spindle region that is densely populated with microtubules. We reveal that spindle elongation prompts microtubules attached to immobile polar chromosomes to pivot around the spindle pole, enabling chromosome contact with the spindle surface. From a functional perspective, we demonstrate a critical role of spindle elongation-driven pivoting in preventing mitotic errors in specific healthy and cancer cells.

Results

Polar chromosomes require a unique congression step to transit across the spindle pole

Given that chromosomes located behind the spindle pole at NEBD take longer to congress to the metaphase plate in comparison to other chromosomes (Klaasen et al., 2022), we hypothesized that they require a specific congression step. Alternatively, they may exhibit a

slower progression of the steps shared with other chromosomes. To distinguish between these possibilities, we imaged human retinal pigment epithelium (RPE1) cells with labeled centromeres and either tubulin or centrosomes using a synergy of STED immunofluorescence (Figure 1A) and LLS live-cell imaging (Figure 1B). Whereas STED microscopy enabled visualization of microtubules within the polar region in super-resolution (50-100 nm range, Supplementary Figure 1A), LLS microscopy enabled imaging of all kinetochores throughout mitosis at a high time resolution (6 seconds) due to the low phototoxicity of this technique, as indicated by the timely onset of anaphase in all cells (Video 1).

By using LLS movies (Figure 1B), we found that at NEBD, 15 ± 2 chromosomes per cell (all data are given as Mean ± SEM, n = 24 cells) were located behind the spindle poles (Supplementary Figure 1B-D). Out of those 15, 8 ± 1 ended their centripetal movement in the region between the two poles, whereas 7 ± 1 chromosomes ended their centripetal movement in the region behind the pole (see examples in Figure 1A and Supplementary Figure 1B). We refer to the latter group as polar chromosomes. By constructing a timeline of the polar chromosome movements (Figure 1B-C, individual stages are most clearly visible in Figure 1A), we found that after NEBD a typical polar chromosome started its centripetal movement approaching the spindle pole from the back until it reached a relatively stable distance from the pole at 3.4 ± 0.2 minutes, which roughly corresponds to the formation of the prometaphase chromosome ring around the nascent spindle (Magidson et al., 2011). Remarkably, the polar chromosomes did not reach the spindle surface, the event we refer to as landing, until 7.4 ± 0.3 minutes after NEBD (Figure 1B-C). During this 4-minute gap, the spindle rapidly elongated and other chromosomes have already started congressing to the metaphase plate. Once the polar chromosomes reached the spindle surface, they immediately started traveling towards the spindle midplane, finishing aligning at 12.3 ± 0.3 minutes (Figure 1B-C, Supplementary Figure 1E).

The observed time gap may be specific to the location of polar chromosomes behind the pole in prometaphase; however, alternatively, it may be due to their large distance to the spindle midplane. To discriminate between these possibilities, we compared the timing of polar and non-polar chromosomes with a similar initial distance to the centrosome midpoint (Supplementary Figure 1F). We found that only polar chromosomes showed a delay in landing and a time gap from the end of the centripetal movement to the attachment to the spindle surface, indicating that the gap is specific to chromosome location (Supplementary Figure 1G-H). The other segments of the chromosome's travel, namely the centripetal movement and the transfer along the spindle surface, lasted similarly for polar and non-polar chromosomes (Supplementary Figure 1I-J), which argues against their contribution to the late alignment. Thus, the delayed alignment of polar chromosomes causing their susceptibility to missegregation is due to a time gap wherein the polar chromosome traverses across the pole to reach the main spindle surface. This reveals an additional step in congression specific to polar chromosomes (Figure 1D).

To test whether this additional step includes the attachments to microtubules, we used STED images (Figure 1A) and found that 58.1 ± 3.2 % of chromosomes already had microtubules next to their kinetochores at a time close to NEBD, whereas 41.9 ± 3.2 % were completely unattached (Supplementary Figure 1K-L). By the end of the centripetal movement phase all kinetochore pairs were attached to microtubules and remained attached throughout the subsequent phases of congression (Supplementary Figure 1K-L). Some of the chromosomes that were unattached and located behind the pole at NEBD might have remained unattached as they were passed by the moving centrosome, resulting in their first contact with spindle microtubules between the spindle poles. In contrast, all polar chromosomes, which made the first contact behind the pole, were attached to microtubules during the transit across

the pole. Thus, the mechanism of pole crossing by the polar chromosomes includes kinetochore-microtubule attachments.

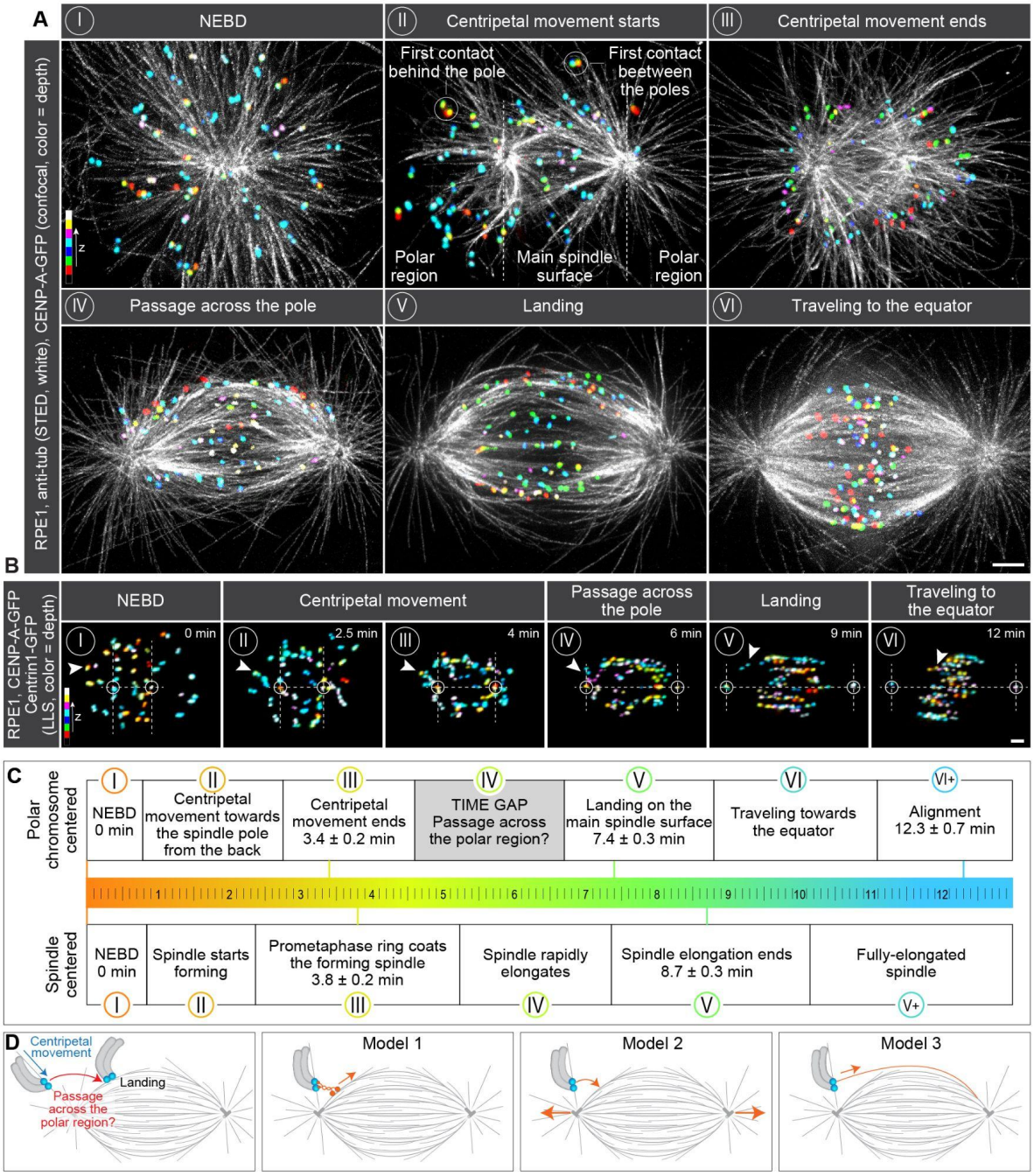

Figure 1. Polar chromosomes require an additional congression step to pass the polar region. **(A)** STED superresolution images of microtubules immunostained for α-tubulin (white) in RPE1 cells stably expressing CENP-A-GFP (colorful, confocal). Images show maximum intensity projections of the whole cell. Kinetochores are color-coded for depth with the brgbcmyw LUT in ImageJ throughout 8-12 z-planes in prometaphase and 35 z-planes in metaphase, correspoding to 2.4-3.6 µm and 10.5 µm, respectively. The images represent different phases of mitosis (I – nuclear envelope breakdown (NEBD), II – a spindle starts forming and kinetochores in the polar region start their centripetal movement towards the spindle pole from the back, III – a prometaphase ring forms and centripetal movement of kinetochores ends, IV – a spindle rapidly elongates while kinetochores located at the back of the pole pass the polar region, V – spindle elongation ends and all kinetochores land onto the spindle

surface, VI – a spindle is fully elongated and kinetochores travel towards the spindle equator). The polar region and the main spindle surface are denoted in image II. **(B)** Time-lapse images of RPE1 cells stably expressing CENP-A-GFP and Centrin1-GFP (colorful, lattice light-sheet). Images show maximum intensity projections of the whole cell. Kinetochores are color-coded for depth with the brgbcmyw LUT in ImageJ throughout 32-40 z-planes, corresponding to 4.6-5.8 µm. Mitotic phases from I to VI correspond to the ones described in (A). The polar region is denoted as a region behind two dashed lines perpendicular to the long spindle axes. Centrosomes are denoted with white circles. White arrows represent one polar kinetochore pair tracked from NEBD until alignment to the spindle equator. **(C)** Polar chromosome-centered (upper) and spindle-centered (lower) timelines of prometaphase events. Events are marked with roman numerals that correspond to the ones shown in (A) and (B). The times are calculated based on 39 kinetochore pairs in 20 cells from 8 experiments. **(D)** Schematic representation of the first (end of centripetal movement) and the last (landing) known time points between which the time gap and possible passage across the polar region occur. Three possible models for passing the spindle pole. In the first model, polar kinetochores are attached to the motor that brings them onto the spindle body. The second model proposes that spindle elongation drives pivoting of astral microtubules that consequently bring polar kinetochores in front of the spindle pole. In the last model, polar kinetochores attach to microtubules emanating from the opposite pole that bring them onto the spindle surface. **(A,B)** Scale bars, 2 µm.

Passage across the pole occurs independently of the motor proteins implicated in chromosome congression

To uncover the mechanism of the passage across the polar region, we envisioned three models (Figure 1E). In the first model, motor proteins located at the kinetochore (CENP-E or dynein) or on the arm (chromokinesins) of the polar chromosomes attach to the microtubules of the main spindle surface and pull the polar chromosome in the direction of the spindle surface. In the second model, the spindle elongates, causing both poles to move outward, thereby repositioning chromosomes from the back of the spindle pole to the main spindle surface. In the third model, microtubules from the opposite side of the spindle attach to the polar chromosome and pull it towards the main spindle surface.

To test the first model, we depleted CENP-E (kinesin-7) (Barisic et al., 2014; Cai et al., 2009; Kapoor et al., 2006; Maiato et al., 2017), Spindly, which promotes dynein recruitment to kinetochores in early mitosis (Griffis et al., 2007), or co-depleted the chromokinesins KIF4A (kinesin-4) and Kid (kinesin-10) (Mazumdar et al., 2004; Wandke et al., 2012; Yajima et al., 2003) by using small interfering RNAs (siRNAs) (Supplementary Figure 2A). We also perturbed actomyosin contraction (Booth et al., 2019; Plessner et al., 2019) by depolymerizing actin via Latrunculin A (Supplementary Figure 2A), thereby completing the test of all motor-driven mechanisms that were previously implied in chromosome congression. Even when said proteins were effectively depleted or inhibited, as determined by a ~90 % reduction of their signal on the spindle, absence from the expected location, and the characteristic phenotype (Supplementary Figure 2B-C), nearly all polar chromosomes successfully traveled from the back of the spindle towards the main spindle surface (Supplementary Figure 2D). A tiny fraction (~2 %) of them after Spindly depletion remained behind the pole, as they were vigorously ejected away from the pole and into the region that surpasses the area of the future spindle, thus indicating the importance of proximity to the pole for successful passage across the pole (Supplementary Figure 2E). Given that Spindly is also essential for the expansion of the kinetochore fibrous corona (Pereira et al., 2018; Sacristan et al., 2018), these data show that the expanded corona is dispensable for the initial chromosome transit across the pole. Taken together, these results show that the passage across the pole occurs independently of the previously described congression drivers, but benefits from the role of dynein in keeping the chromosomes close to the spindle pole.

Pivoting of astral microtubules around the centrosome repositions polar chromosomes close to the spindle surface

We next considered the second model, where spindle elongation causes pivoting of astral microtubules attached to polar chromosomes towards the main spindle surface. To test this model, we tracked in 3D the polar kinetochores and their microtubules, as well as centrosomes and chromosome arms, from the end of the centripetal movement until after landing on the spindle surface (Figure 2A-C, Supplementary Figure 2F). To quantify the pivoting motion of a polar chromosomes, we defined its pivoting angle as the angle between the centrosome-centrosome axis and the line connecting the sister kinetochores midpoint with the centrosome (Figure 2D). The pivoting angle showed a fast decrease during the period of rapid spindle elongation and stabilized as the spindle length stabilized (Figure 2E-F). Moreover, the pivoting angle was strongly anti-correlated with the spindle length for individual kinetochore pairs (Figure 2G, Supplementary Figure 2G). These results support the spindle elongation-driven pivoting model.

To explore the pivoting motion of astral microtubules, which are undetectable in the typical videos of mitosis, we developed a confocal microscopy protocol with adjusted pixel size (See Methods) to image RPE1 cells expressing EYFP-α-tubulin with added HaloTag-CENP-A (Figure 2A). We found that the kinetochores of a polar chromosome were adjacent to a microtubule signal representing a single astral microtubule, or a few in a bundle. This astral microtubule pivoted around the centrosome in the direction of the spindle surface, while maintaining its connection to the polar chromosome, during the centrosome's movement outwards (Figure 2A and 2H-I). The microtubules were straight instead of bent (Supplementary Figure 2H), indicating that the entire microtubule pivots around the centrosome, as opposed to solely the plus-end-proximal segment gliding along the cell cortex or organelles. We also observed pivoting of chromosome-attached astral microtubules in an osteosarcoma cell line (U2OS) with the GFP-tagged microtubule plus-end marker EB3 (Stepanova et al., 2003), which suggests that the transit across the pole involves pivoting also in cancer cells (Supplementary Figure 2I). Overall, the direct observation of the microtubule pivoting motion around the centrosome supports the pivoting model and indicates that the force driving the pivoting of the chromosome-attached microtubule exceeds the force preserving the microtubule extension direction at the centrosome.

In contrast to the chromosome-carrying astral microtubules, the microtubules that were not attached to a chromosome did not exhibit directed pivoting but instead pivoted around the centrosome in a random manner (Figure 2B and 2H-I, Supplementary Figure 2J-K). Their pivoting was similar in the cases when their centrosome moved significantly and when it was stationary (Figure 2B and 2H-I, Supplementary Figure 2J-L). Whereas chromosome-carrying microtubules pivoted by ~36 degrees, on average, in 3 minutes, the chromosome-free microtubules changed their angle by less than ~8 degrees (Supplementary Figure 2J). These findings indicate that the force driving the pivoting of chromosome-free microtubules is independent of the centrosome movement and smaller than the force maintaining their direction at the centrosome.

A key assumption of the pivoting model is that larger objects show a larger resistance to the movement through the cytoplasm. This implies that, during spindle elongation, a larger chromosome should move less and thus its microtubule should pivot more than that of a smaller chromosome. A temporal maximum-intensity projection of spindles labeled with EB3-GFP and H2B-mCherry showed indeed that chromosomes were stationary while the centrosomes moved outwards during spindle elongation (Figure 2C). Moreover, when we compared a

smaller and a larger chromosome connected to the same pole, we found that the smaller chromosome slightly moved together with the centrosome whereas the larger one remained relatively immobile (Supplementary Figure 2M), resulting in a faster decrease of the pivoting angle for larger chromosomes (Supplementary Figure 2N-P). Collectively, these findings support the model in which spindle elongation induces pivoting of astral microtubules attached to stationary polar chromosomes (Figure 2J), enabling their interaction with the spindle surface.

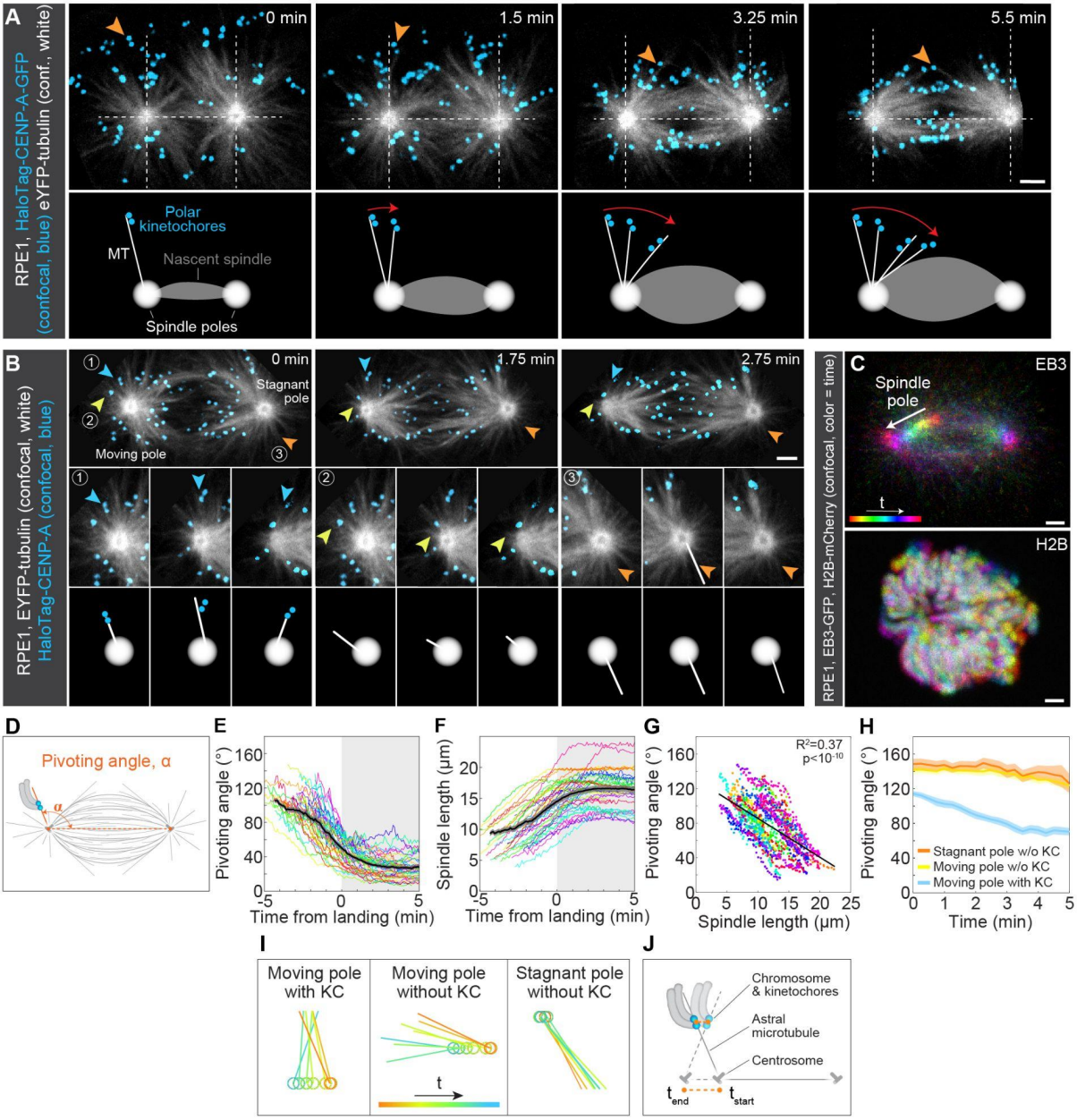

Figure 2. Polar chromosomes rely on spindle elongation-driven pivoting of astral microtubules to pass the polar region. **(A)** Upper panel: time-lapse images of RPE1 cells stably expressing EYFP-tubulin (white, confocal) and H2B-mRFP (not imaged) with added HaloTag-CENP-A (blue, confocal). Each image represents a single central z-plane. The orange arrow denotes the kinetochore pair attached to the pivoting astral microtubule. Lower panel: Schematic representation of pivoting based on the images from the upper panel. The position of the left centrosome is fixed throughout the schemes. **(B)** Time-lapse images of RPE1 cells stably expressing EYFP-tubulin (white, confocal) and H2B-mRFP (not imaged) with added HaloTag-CENP-A (blue, confocal). Moving and stagnant spindle poles are

denoted in the first image. The blue arrow represents the microtubule attached to the polar kinetochore tracked over time. Yellow and orange arrows represent microtubules without attached polar kinetochores on the moving and stagnant spindle pole, respectively. Insets and schematic representations of the previously described microtubule types are shown below the images of the whole spindle. Spindle poles on insets are depicted with a black cross. Images are maximum intensity projections of 3 central z-planes, corresponding to 3 µm. **(C)** Images of RPE1 cells stably expressing EB3-GFP (colorful, confocal, left image) and H2B-mCherry (colorful, confocal, right image). Images are temporal maximum intensity projections of the centrosome (left) and chromosome (right) movements over 3 central z-planes (3 µm) and a time period of 3.3 minutes, color-coded for time with the Spectrum LUT in ImageJ. Chromosomes are depicted with white arrows. **(D)** Schematic representation of measured parameters for polar kinetochores along with the starting (end of centripetal movement) and last (landing) tracking point (t = 0 minutes). Spindle length was determined as the distance between the two spindle poles. The pivoting angle was determined as an angle that the midpoint of the kinetochore pair closes with the long spindle axis. **(E)** The pivoting angle of polar kinetochore pairs and **(F)** corresponding spindle length in time. The landing point of each kinetochore pair is set to zero. Values are shown as mean (dark line) and SEM (shaded areas). N = 39 kinetochore pairs in 20 cells from 8 experiments. **(G)** Anticorrelation of the pivoting angle and spindle length for the same polar kinetochores as in (E). Each color represents one polar kinetochore pair and each dot represents its pivoting angle and the corresponding spindle length in time. Linear regression. N = 39 kinetochore pairs in 20 cells from 8 experiments. **(H)** The pivoting angle of the microtubule attached to the kinetochores on the moving pole (blue), microtubule without attached kinetochores on the moving pole (yellow) and microtubule without attached kinetochores on the stagnant pole (orange) in time. Values are shown as mean (dark line) and SEM (shaded areas). N = 16 microtubules with polar kinetochores attached to them on the moving pole in 10 cells from 4 experiments. N = 16 microtubules without polar kinetochores attached to them on the moving pole in 10 cells from 4 experiments. N = 14 microtubules without polar kinetochores attached to them on the stagnant pole in 6 cells from 4 experiments. The fourth group, microtubules with polar kinetochores attached to them on the stagnant pole could not be found, as poles were stagnant only when they were already at the nuclear border at NEBD and, therefore, had no polar chromosomes to begin with. **(I)** Schematic representation of the spindle pole movement and pivoting angle for each microtubule marked in (B) in time (from red to blue). Note that only the microtubule attached to polar kinetochores pivots around the spindle pole. **(J)** Schematic representation of the centrosome, astral microtubule and chromosome movements during pivoting. Note that the centrosome moves significantly while microtubules pivot under the weight of a chromosome which moves only slightly. **(A-C)** Scale bars, 2 µm.

Direction of the centrosome movement dictates the direction of microtubule pivoting

The pivoting model provides a straightforward prediction: if the spindle dynamics reverses from elongation to shortening, the direction of microtubule pivoting should also reverse, implying that microtubules should pivot towards the region behind the spindle pole instead of towards the main spindle surface. Similarly, a constant spindle length should be associated with negligible pivoting. To test these predictions, we designed a set of manipulations of Eg5/KIF11 (kinesin-5), the main motor protein driving spindle elongation (Kapitein et al., 2005; Kashina et al., 1997), to either reverse, restore, or block spindle elongation (Figure 3A-D).

To reverse spindle elongation into shortening, we added the Eg5 inhibitor STLC (S-Trityl-L-Cysteine) (Skoufias et al., 2006) during prometaphase at a point when the spindle had formed, and the kinetochores of polar chromosomes approached the main spindle surface but had not yet attached to it. After the addition of STLC, the spindle started shortening, and the kinetochores of the polar chromosomes that were already close to the spindle surface started pivoting towards the back of the spindle (Figure 3B). This reversed pivoting was evident as an increase in the pivoting angle during spindle shortening in STLC-treated cells, in contrast to the decrease of the pivoting angle during spindle elongation in untreated cells (Figure 3E-F,

Supplementary Figure 3A-C). Remarkably, the pivoting direction was reversible, moving back and forth (Figure 3D). The washout of the Eg5 inhibitor monastrol (Mayer et al., 1999) reversed the inhibitor-induced spindle shortening into elongation, which triggered kinetochore pivoting towards the main spindle surface (Figure 3G, Supplementary Figure 3D-E), in agreement with the predictions from the model.

To block spindle elongation, we added the ATP-competitive Eg5 inhibitor FCPT (2-(1-(4-fluorophenyl)cyclopropyl)-4-(pyridin-4-yl)thiazole) (Groen et al., 2008; Rickert et al., 2008), which induces tight binding of Eg5 onto microtubules. Subsequently, the spindle length remained constant, and the kinetochores of polar chromosomes did not pivot significantly, providing further support to the model (Figure 3C and 3E-F, Supplementary Figure 3A-B and 3F). Finally, to exclude the possibility that the observed effects of Eg5 inhibitors were due to roles of Eg5 other than driving spindle elongation, we employed an orthogonal approach. This involved adding a low dose of nocodazole (20 nM), which induces mild spindle shortening after NEBD while preserving the attachments of chromosomes to astral microtubules (Rajendraprasad et al., 2021). In agreement with the results from Eg5 inhibition, spindle shortening caused an increase in the number of kinetochores behind the pole (Supplementary Figure 3G-I). Collectively, these data show that the centrosome movement due to spindle elongation or shortening dictates the direction of kinetochore pivoting.

To quantitatively test our model, we explored whether the extent of pivoting can be explained by the extent of spindle elongation or shortening. A strong correlation between the change in spindle length and the simultaneous change in the pivoting angle supports this notion (Figure 3H). Moreover, we calculated the expected change in the pivoting angle for a given change in the spindle length, assuming immobile chromosomes (see Methods and Supplementary Figure 3J). The resulting theoretical prediction closely matched the linear fit of the data (Figure 3H). Taken together, our results reveal spindle elongation as a necessary and sufficient driver of chromosome passage across the spindle pole, dictating both the direction and magnitude of pivoting of chromosome-carrying astral microtubules (Figure 3I).

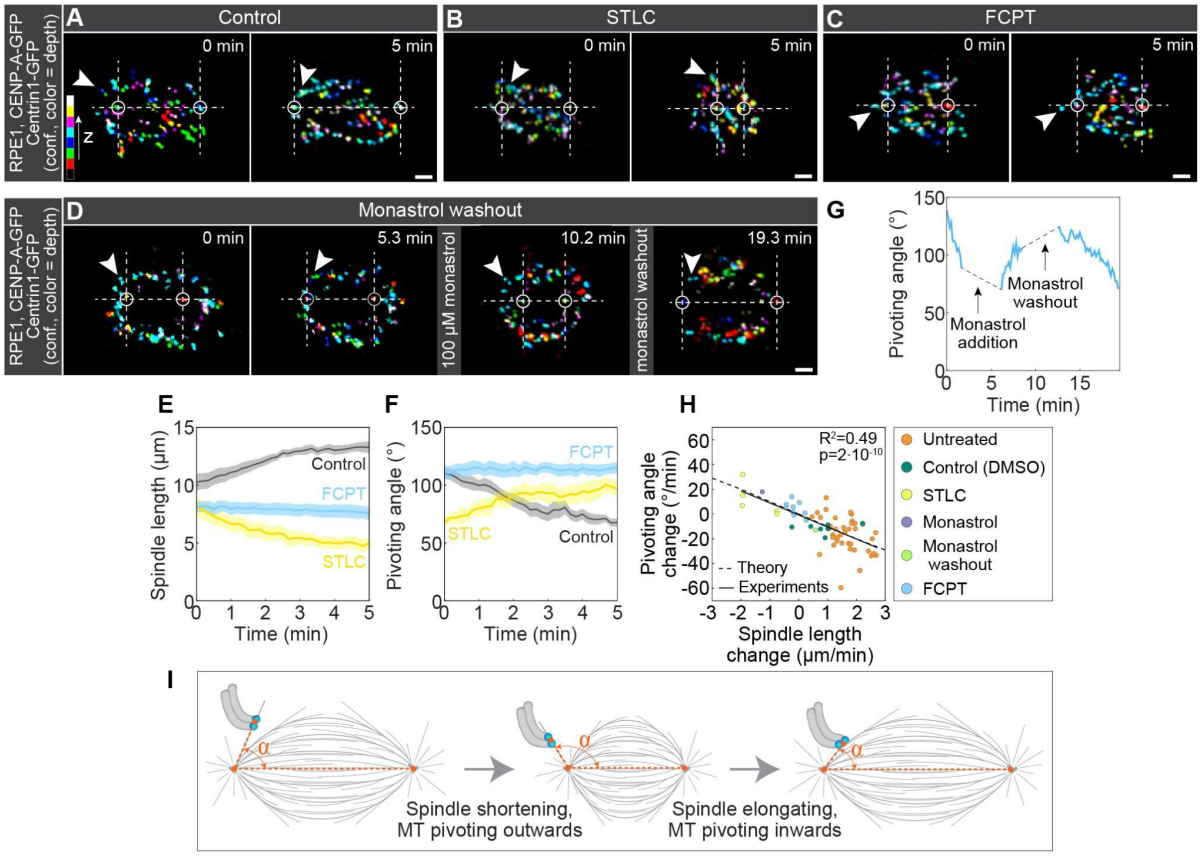

Figure 3. Centrosome movement determines the direction and magnitude of pivoting. **(A-D)** Time-lapse images of RPE1 cells stably expressing CENP-A-GFP and Centrin1-GFP (colorful, confocal) for (A) DMSO control, (B) STLC-, (C) FCPT-, and (D) monastrol-treated cells. White arrows represent one polar kinetochore pair over time. White circles represent spindle poles, horizontal dashed lines represent the long spindle axis and lines perpendicular to it denote the borders of the polar region. Note that the STLC treatment caused spindle shortening, FCPT treatment blocked spindle elongation, whereas monastrol treatment caused spindle shortening that could be reversed by washout. Kinetochores are color-coded for depth with the brgbcmyw LUT in ImageJ throughout 14-21 z-planes, correspoding to 5.6-8.4 µm. **(E)** Spindle length and **(F)** pivoting angle in time for polar kinetochores in control (gray), STLC (yellow) and FCPT (blue) treatment. Values are shown as mean (dark line) and SEM (shaded areas). t = 0 minutes corresponds to inhibitor addition and activity. N = 7 kinetochore pairs in 7 cells from 7 experiments (DMSO), N = 5 kinetochore pairs in 3 cells from 3 experiments (STLC), N = 9 kinetochore pairs in 7 cells from 7 experiments (FCPT). **(G)** Change of pivoting angle in time during the monastrol washout experiment. Dashed lines denote the time required for the addition or washout of the inhibitor together with the time required for the spindle length to start changing. N = 1 kinetochore pair in 1 cell from 1 experiment. **(H)** The experimental correlation of the pivoting angle change and spindle length change for the control (orange), DMSO control (dark green), monastrol washout (light green), FCPT (blue), monastrol (purple) and STLC (yellow) treatments along with the theoretical curve calculated based on the experimental parameters from DMSO and STLC experiments (See Supplementary Figure 3). Linear regression. **(I)** Schematic representation of pivoting angle change based on the spindle length change. **(A-D)** Scale bars, 2 µm.

Polar chromosomes form complex attachments yet remain bound to the same microtubule during pivoting

Prior to establishing end-on attachments, kinetochores initially bind to microtubules laterally (Alexander and Rieder, 1991; Magidson et al., 2011; Shrestha and Draviam, 2013). To explore the types of attachments polar kinetochores form with astral microtubules during their pivoting, and whether they transition between different microtubules, we imaged microtubules by STED microscopy in RPE1 cells expressing CENP-A-GFP, at various stages between the end of centripetal movement and landing (Figure 4A). Remarkably, rather than primarily observing lateral attachments, we found a wide variety of attachment types, including lateral, monotelic, and syntelic configurations, together with more complex and previously unidentified types (Figure 4A). We define them as: 1) bilateral, when two sister kinetochores attach laterally to two astral microtubules, 2) mono-lateral, when one sister kinetochore has an end-on attachment in addition to both sisters being laterally attached to the same astral microtubule, 3) mono-bilateral, as a combination of bilateral and one end-on attachment, and 4) syn-lateral, as a combination of syntelic and one lateral attachment. Mono-lateral attachments were the most frequent, followed by lateral and bilateral ones (Figure 4B).

Accordingly, the kinetochore further away from the pole had more Mad2, which marks kinetochores with missing or unstable end-on attachments (Kuhn and Dumont, 2017; Waters et al., 1998), compared to its sister (Figure 4C-D and Supplementary Figure 4A). This suggests that the further kinetochore typically forms a lateral attachment, whereas the closer one forms an end-on attachment in addition to the lateral one. Mad2 levels at kinetochores with end-on attachments were lower than at those with lateral attachments, but higher than at end-on attached kinetochores in metaphase (Figure 4E), suggesting that these immature end-on attachments in prometaphase represent a future k-fiber that starts forming even as the kinetochore is still located behind the pole.

To explore if chromosomes can switch from one microtubule to another during pivoting, we imaged live cells expressing EYFP-α-tubulin and H2B-mRFP with HaloTag-CENP-A (Supplementary Figure 4B). We found that 63.1 ± 11.1 % of polar chromosomes remained attached to a single microtubule during pivoting, 21.1 ± 9.4 % made one change between microtubules, whereas multiple changes were rare (Figure 4F). Most of the observed changes included only a change for the further kinetochore, whereas the closer one remained attached to the same microtubule during the entire process (Figure 4G and Supplementary Figure 4B). Thus, in a typical case with 7 polar chromosomes, 4 of them remain attached to a single microtubule during pivoting, 2 change the attachment of the further kinetochore, e.g. from lateral to bilateral, whereas 1 shows a more complex transition (Figure 4H). In sum, polar chromosomes make a variety of attachments with astral microtubules but typically remain attached to the same microtubules while crossing the polar region.

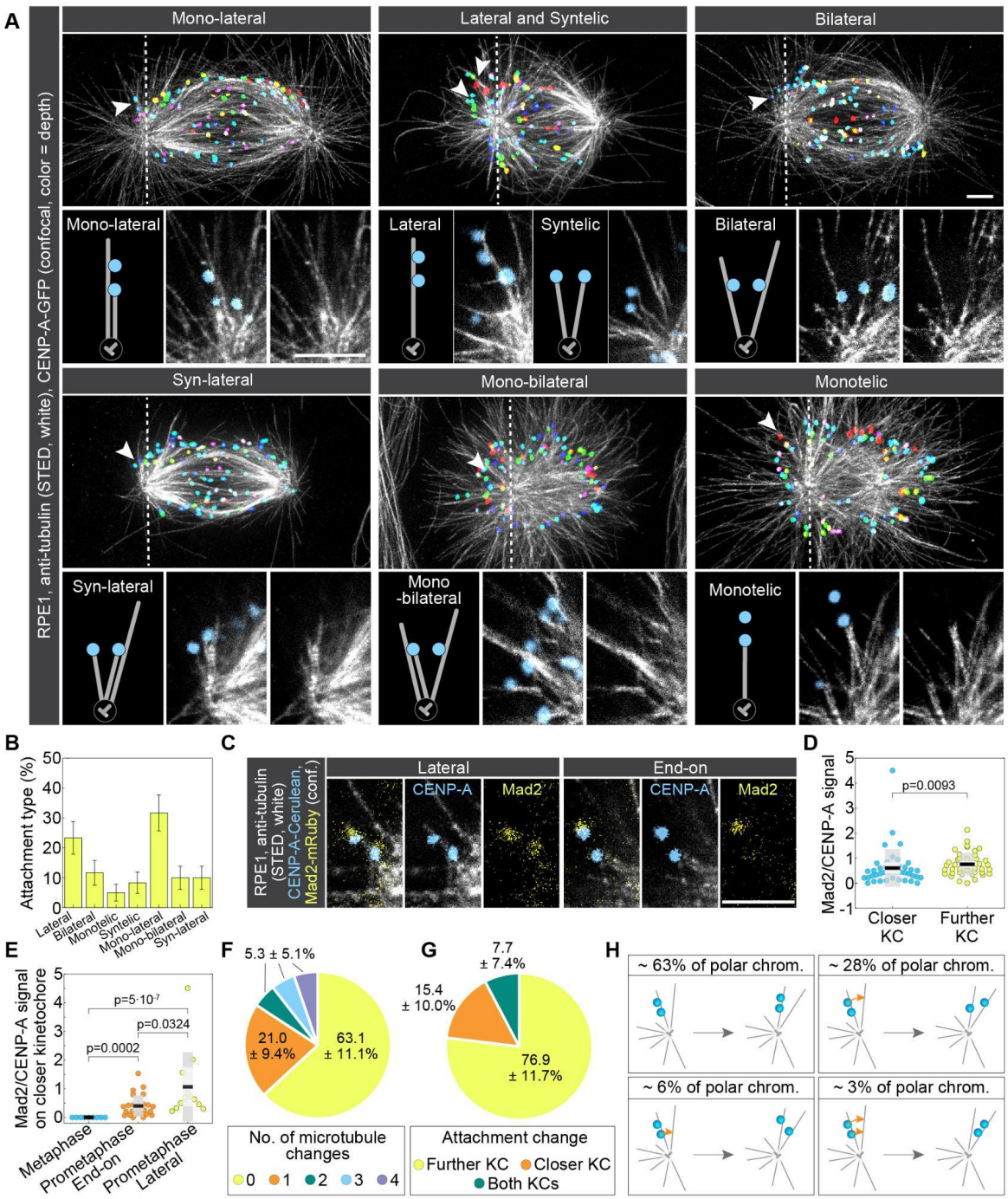

Figure 4. Polar kinetochores form complex attachments with the microtubules they remain attached to during pivoting. **(A)** STED superresolution images of microtubules immunostained for α-tubulin (white) in RPE1 cells stably expressing CENP-A-GFP (colorful, confocal). Images show maximum intensity projections of the whole cell. Kinetochores are color-coded for depth with the brgbcmyw LUT in ImageJ throughout 8-17 z-planes, corresponding to 2.4-5.1 µm. White arrows represent a kinetochore pair attached to microtubules shown in insets below the image. Insets show single z-planes or maximum intensity projections of 2-3 z-planes where the microtubule of interest is located, smoothed with 0.75-mm-sigma Gaussian blur. The schematic representations of different attachment types are shown next to the associated insets. **(B)** Fractions of different attachment types for polar chromosomes between the end of the centripetal movement and landing quantified from STED images. N = 60 kinetochore pairs in 24 cells from 5 experiments. **(C)** STED superresolution images of

polar chromosomes attached to microtubules immunostained for α-tubulin (white) in RPE1 cells stably expressing CENP-A-Cerulean (blue) and Mad2-mRuby (yellow). Images show a single z-plane, with kinetochores and microtubules smoothed with 0.75-mm-sigma Gaussian blur. Intensities of CENP-A and Mad2 are equally adjusted throughout the images. **(D)** Univariate scatter plot of the relative Mad2/CENP-A signal for closer (blue) and further (yellow) polar kinetochore. Measurements were done on STED images as from (C). N = 42 kinetochore pairs in 29 cells from 3 experiments. Statistical test: Mann-Whitney U test. **(E)** Univariate scatter plot of the relative Mad2/CENP-A signal for closer polar kinetochore in metaphase (blue), in prometaphase when the kinetochore makes an end-on attachment (orange) and in prometaphase when the kinetochore makes a lateral attachment (yellow). Measurements are done on STED images as from (C). N = 10 kinetochores from 5 kinetochore pairs in 2 cells from 1 experiment for metaphase, N = 26 end-on attached kinetochores and 12 laterally attached kinetochores in 29 cells from 3 experiments for prometaphase. Statistical test: Kruskal-Wallis with post-hoc Dunn's test. **(F)** Pie chart for the number of microtubule changes during pivoting measured in RPE1 cells stably expressing EYFP-tubulin with added HaloTag-CENP-A (See Supplementary Figure 4). N = 19 kinetochore pairs in 10 cells from 4 experiments. **(G)** Pie chart for attachment changes on further (yellow), closer (blue) and both (green) polar kinetochores measured in the same cells as in (F). N = 13 kinetochore pairs in 5 cells from 3 experiments. **(H)** Schematic representations of types of attachment changes that polar kinetochores (blue circles) undergo during pivoting and their frequencies. The orange arrows denote which kinetochore in a pair changes microtubules during pivoting. **(A,C)** Scale bars, 2 μm.

Microtubules from the opposite side of the spindle rarely help the movement of polar chromosomes

While our results reveal microtubule pivoting as the main mechanism that polar chromosomes use to cross the pole, microtubules extending from the opposite side of the spindle may contribute to this process by pulling the chromosomes towards the main spindle surface (Figure 1E). By using STED microscopy, we found that in phases between the end of centripetal approaching and landing, 30.0 ± 5.9 % of kinetochore pairs in the polar region (i.e. attached to an astral microtubule and within ~3 μm from the spindle pole) were next to a microtubule extending from the opposite side of the spindle (Figure 5A), whereas 70.0 ± 5.9 % had no such microtubule nearby (Figure 5B). Attachments to microtubules from the opposite spindle half were rare behind the pole, seen in only 20.5 ± 6.5 % kinetochore pairs, but were more frequent in the region in front of the pole, where 47.6 ± 10.9 % of kinetochore pairs showed attachments before joining the main spindle surface (Figure 5B). These attachments were predominantly end-on (Figure 5C, Supplementary Figure 5A). Most of these microtubules had tubulin intensity similar to that of astral microtubules, suggesting they are single microtubules (Supplementary Figure 5B).

If the microtubules from the opposite side pull the chromosome across the pole, this is expected to cause an increase of both the interkinetochore distance and of the distance between the kinetochores and the closer pole. We found such changes within one minute before landing (Supplementary Figure 5C-D), when the kinetochores are typically close to the main spindle surface (at an angle <60 degrees, see Figure 2E), suggesting that the pulling by microtubules from the opposite side contributes only to the last part of the chromosome movement towards the spindle surface. Live-cell STED microscopy provided direct visualization of the process in which such kinetochores attain end-on attachment to a microtubule extending from the opposite spindle half, followed by an increase in interkinetochore distance and movement towards the opposite pole (Supplementary Figure 5E). These findings show that in rare instances, microtubules extending from the opposite side of the spindle can pull the chromosome, especially when it is already close to the spindle surface. Together, our results suggest that of the 7 polar chromosomes, around 5 cross the polar region and reach the main spindle surface

only by pivoting, 1-2 are pulled by microtubules from the opposite side after the initial pivoting motion, whereas <1 chromosome per cell interacts with microtubules from the opposite side before pivoting (Figure 5E).

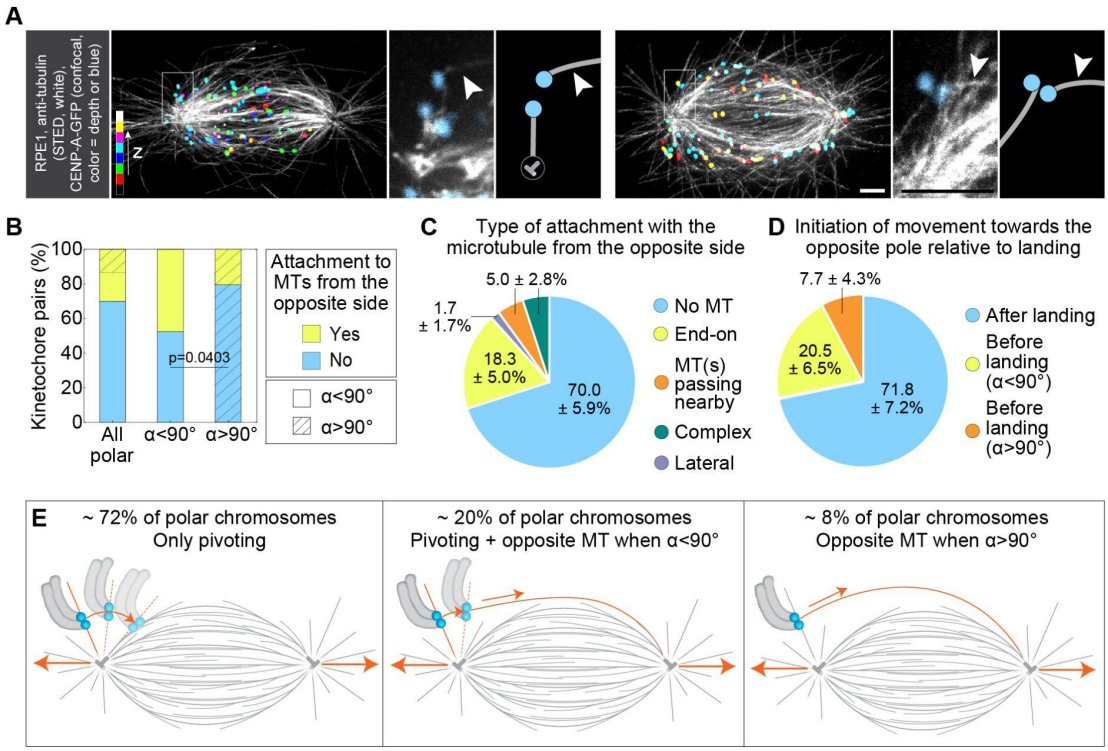

Figure 5. Microtubules from the opposite side of the spindle are dispensable for passage across the pole. (A) STED superresolution images of microtubules immunostained for α-tubulin (white) in RPE1 cells stably expressing CENP-A-GFP (colorful, confocal). Images show maximum intensity projections of the whole cell. Kinetochores are color-coded for depth with the brgbcmyw LUT in ImageJ throughout 16 and 9 z-planes, corresponding to 4.8 and 2.7 µm, respectively. White squares represent a polar kinetochore attached to the microtubule from the opposite side of the spindle. Insets with the associated schemes are shown next to the image of the whole spindle. White arrows denote the microtubule coming from the opposite side of the spindle. Insets are maximum intensity projections of 2 and 3 z-planes where the microtubule of interest is located, smoothed with 0.75-mm-sigma Gaussian blur. **(B)** Percentages of kinetochores that are unattached (blue) or attached to the microtubule from the opposite side of the spindle (yellow) measured in cells as in (A). The shaded area represents kinetochores located at the angle above 90° with respect to the long spindle axis. N = 18 kinetochore pairs in 15 cells from 5 experiments. Statistical test: Fisher's exact test. **(C)** Pie chart representing the percentage of different attachment types with the microtubule from the opposite side. N = 18 kinetochore pairs in 15 cells from 5 experiments. **(D)** Pie chart representing the percentage of polar kinetochores from LLS videos that initiate their movement towards the opposite pole after landing (blue), before landing at an angle below 90° (yellow) and before landing at an angle above 90° (orange), indicative of a force other than pivoting. N = 39 kinetochore pairs in 20 cells from 8 experiments. **(E)** Schematic representation of percentages of polar chromosomes that pivot without forming an attachment to the microtubule from the opposite side before landing (left), that pivot and attach to microtubule from the opposite side once they reach the angle below 90° (middle) and the ones that attach to microtubule from the opposite side at the angle above 90° (right). **(A)** Scale bars, 2 µm.

Incomplete spindle elongation leads to delayed chromosome passage across the pole and mis-segregation

To explore the functional relevance of the pivoting model, we asked whether perturbations of this mechanism lead to chromosome segregation errors. We reasoned that inducing premature anaphase onset by using AZ3146 (Figure 6A), a small-molecule inhibitor of the mitotic kinase Mps1 (Hewitt et al., 2010), would not only lead to chromosome segregation errors due to perturbed attachment error correction and the spindle assembly checkpoint response, but may also result in incomplete spindle elongation. This should in turn lead to incomplete passage of polar chromosomes across the pole, allowing us to explore the consequences of perturbed pole crossing on the segregation fidelity of these chromosomes.

The chromosomes that were polar at NEBD mis-segregated more frequently than non-polar chromosomes that are similarly positioned with respect to the nucleus and the centrosome midpoint (Figure 6B) (Klaasen et al., 2022). Whereas polar and non-polar chromosomes were similar in the frequency of misaligned and lagging chromosomes, there was a stark difference in the fraction of unaligned chromosomes (Figure 6B). About 20% of polar chromosomes with erroneous segregation remained unaligned throughout mitosis, leading to aneuploid daughter cells. In contrast, such cases were absent in the non-polar group (Figure 6B). These results suggest that the mis-segregation bias towards polar chromosomes is largely caused by their persistent unalignment.

Among the chromosomes with erroneous segregation, the persistently unaligned chromosomes were the last ones to pass from the back to the front of the spindle pole (Supplementary Figure 6A), suggesting that the cause for their unalignment lies in perturbed pivoting around the pole. Based on our model, we expect that the cells that entered anaphase with persistently unaligned chromosomes had less extensive spindle elongation than those without unaligned chromosomes. Indeed, we found that the spindles with persistently unaligned chromosomes elongated more slowly, entering anaphase at a ~4 µm shorter length than the spindles without such chromosomes (Figure 6C, Supplementary Figure 6B-C). Different timing of anaphase was not the cause of persistent unalignment, as the spindles with and without unaligned chromosomes entered anaphase at a similar time (17.8 ± 2.5 vs. 17.9 ± 0.9 minutes). These data suggest that the missegregation bias towards polar chromosomes mainly stems from their propensity to remain unaligned, which is higher in cells with slower spindle elongation and, thus, ineffective chromosome passage across the pole.

To link the pivoting model with chromosome identity, we tested whether this model can explain the frequent missegregation of certain chromosomes, in particular chromosome 1, observed across various treatments and cancer types (Klaasen et al., 2022; Worrall et al., 2018). We set out to determine the „danger zone“ – a zone within the interphase nucleus that would predispose chromosomes to mis-segregate as persistently unaligned. We found that most of the cells align the centrosomes along the long nuclear axis during prometaphase (79.17 ± 8.29 %, Figure 6D-E, Supplementary Figure 6D-E), which in turn is mostly aligned with the long cellular axis (Supplementary Figure 6F) (Stiff et al., 2020). This suggests that the „danger zone“ is situated in the nuclear caps, i.e., regions near the ends of the major axis of the nucleus (Figure 6F), because the chromosomes located there in interphase typically end up behind the centrosome in early mitosis. We then compared interphase positions of chromosome 1, which shows a strong missegregation bias, with interphase positions of chromosome 9, which has a missegregation probability that corresponds to random error frequency (Klaasen et al., 2022) (Figure 6D and 6G). Remarkably, we found that chromosome 1 resides in the „danger zone“ in 71.00 ± 2.78 % of cases. In contrast, chromosome 9 resides in the „danger zone“ in only 45.83 ± 5.87 % of cases (Figure 6G). These findings support the idea that the missegregation

bias of chromosome 1 arises from its preferential position in interphase within the nuclear caps. Chromosomes located in this "danger zone" are susceptible to failure in crossing the pole, leading to their persistent unalignment during mitosis.

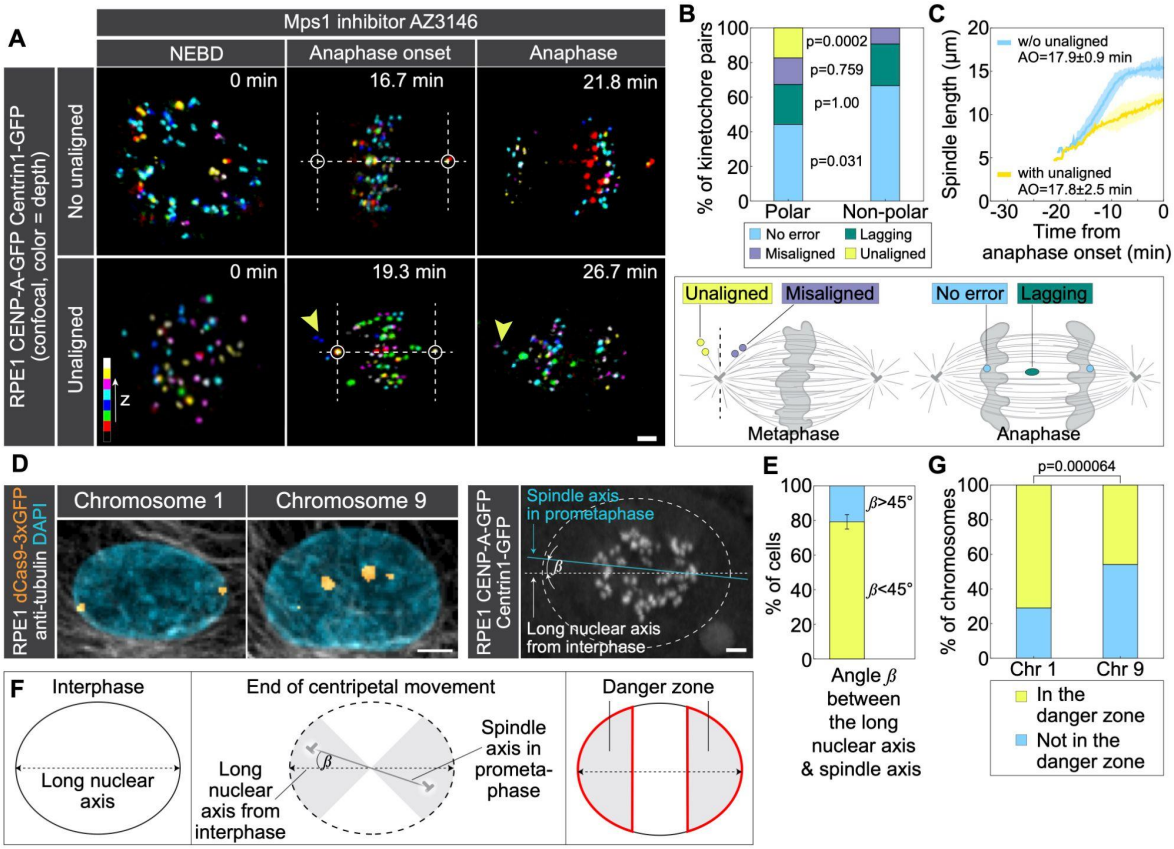

Figure 6. Incomplete spindle elongation compromises passage across the pole for polar chromosomes located in the danger zone. (A) Time-lapse images of RPE1 cells stably expressing CENP-A-GFP and Centrin1-GFP (colorful, confocal) and treated with Mps1 inhibitor AZ3146. The images show maximum intensity projections of the imaged cells. The upper panel represents cells without unaligned chromosomes and the lower panel represents cells with unaligned chromosomes. Kinetochores are color-coded for depth with the brgbcmyw LUT in ImageJ throughout 14-21 z-planes, corresponding to 5.6-8.4 µm. **(B)** Percentage of polar (left bar) or non-polar (right bar) kinetochore pairs that segregated normally (no error, light blue) or ended up as lagging (green), misaligned (dark blue) or unaligned (yellow) kinetochores. Each group of kinetochores is depicted on the scheme below the graph. N = 52 polar kinetochore pairs in 7 cells from 4 experiments. N = 54 non-polar kinetochore pairs in 7 cells from 4 experiments. Statistical test: Fisher's exact test. **(C)** Spindle length in time for cells treated with AZ3146 divided into those that have (orange) or do not have (blue) unaligned chromosomes at anaphase onset. Values are shown as mean (dark line) and SEM (shaded areas). N = 3 cells with unaligned chromosomes from 2 experiments. N = 4 cells without unaligned chromosomes from 2 experiments. **(D)** Left panel: still images of the nucleus in interphase in RPE1 cells stably expressing dCas9-3xGFP (orange) and stained with anti-α-tubulin (gray) and DAPI (blue). Cells are transduced with lentiviruses for chromosome 1 (left) of chromosome 9 (right). Images are maximum intensity projections of 30 z-planes, corresponding to 15 µm. Right panel: an image of RPE1 cell imaged using lattice light-sheet microscopy at the end of centripetal movement. A dashed circle denotes the approximate position of the former nucleus in interphase (See Supplementary Figure 6 for detailed contours). The white dashed line denotes the position of the former long nuclear axis in interphase. The

blue dashed line denotes the spindle axis in prometaphase at the end of the centripetal movement. The image is a maximum intensity projection of 42 z-planes covering the whole cell, corresponding to 6.1 µm. **(E)** Percentage of cells in which the long spindle axis is roughly parallel to the former long nuclear axis (yellow, below 45°) and cells in which the long spindle axis is roughly perpendicular to the former long nuclear axis (blue, above 45°). N = 24 cells from 8 experiments. **(F)** Schematic representation of the nuclear danger zone in interphase with respect to the position of the spindle axis in prometaphase. Chromosomes are located in the danger zone if they are situated within the 45° angle from the long nuclear axis and relatively close to the nuclear border. **(G)** Percentage of cells with chromosome 1 or 9 located in the nuclear danger zone (yellow) or outside the nuclear danger zone (blue). N = 266 chromosomes in 133 cells from 4 experiments for chromosome 1. N = 72 chromosomes in 36 cells from 3 experiments for chromosome 9. Statistical test: Chi-squared test. **(A,D)** Scale bar, 2 µm.

Unaligned chromosomes in an ovarian cancer cell line can be rescued by improving spindle elongation

Finally, we set out to investigate the role of chromosome pivoting in mitotic fidelity of cancer cells. The pivoting model predicts that cancer cells with poor spindle elongation should have more polar chromosomes, which may be rescued by increasing spindle elongation. To rescue such mitotic errors, we searched the literature for candidate cell lines that show frequent unaligned chromosomes and short spindles (Supplementary Figure 7A) (Barretina et al., 2012; Bird and Hyman, 2008; Cerami et al., 2012; de Bruijn et al., 2023; Gao et al., 2013; Ghandi et al., 2019; Gomes et al., 2022; Klaasen et al., 2022; Kletter et al., 2021; Reinhold et al., 2012; Risteski et al., 2024; Tamura et al., 2020; Tucker et al., 2023). The ovarian carcinoma cell line OVSAHO was identified as the most promising candidate (Figure 7A and Supplementary Figure 7A). In contrast to extensive spindle elongation by ~9 µm between NEBD and metaphase in RPE1 cells, OVSAHO spindles elongated by only ~3 µm (Figure 7B). This was accompanied by the failure of polar chromosomes to escape the polar region (Figure 7A and 7C).

To increase spindle elongation, we used depletion of KIF4A because it increases the spindle length in metaphase in HeLa and RPE1 cells (Jagrić et al., 2021; Risteski et al., 2022). Although depletion of KIF18A also increases spindle length, it was excluded due to high sensitivity of ovarian cancer cell lines to KIF18A inhibition (Gliech et al., 2024). OVSAHO cells depleted of KIF4A showed spindle elongation by ~5 µm, reaching a final metaphase length of 12.74 ± 0.15 µm, in comparison with 11.19 ± 0.11 µm without depletion (Supplementary Figure 7B). Remarkably, we observed a five-fold decrease in the number of cells with unaligned chromosomes (i.e., located behind the pole in metaphase), from 15.63 ± 2.87 % to 3.19 ± 1.40 % after KIF4A depletion (Figure 7C), in agreement with the prediction of our model. At the same time, the number of misaligned chromosomes (i.e., located between the two spindle poles but away from the metaphase plate in metaphase) remained unchanged (Figure 7C), suggesting that they arise due to other previously described causes (Vukušić and Tolić, 2022) and pointing to unaligned chromosomes as a distinct segregation error specifically caused by impaired spindle elongation.

Alternatively, the observed rescue of unaligned chromosomes may be due to the perturbed activity of KIF4A as a chromokinesin that generates polar ejection forces on the chromosomes (Novais-Cruz et al., 2023). However, several lines of evidence argue against this possibility: i) unaligned chromosomes were equidistant to the nearest pole in untreated and KIF4A-depleted cells, indicating no significant difference in polar ejection forces and the associated attachment stabilization (Supplementary Figure 7C, (Chong et al., 2024)); ii) KIF4A depletion resolved unaligned but not misaligned chromosomes (Figure 7C), which are expected to be equally affected by polar ejection forces, whereas spindle elongation is expected to rescue

only unaligned ones; iii) OVSAHO had no initial mutations or expression changes in chromokinesins that would lead to increased polar ejection forces and premature attachment stabilization (Supplementary Figure 7A). In conclusion, our results show that insufficient spindle elongation, resulting in poor microtubule pivoting, leads to frequent unaligned chromosomes in a cancer cell line. These mitotic errors can be directly rescued by increasing spindle elongation.

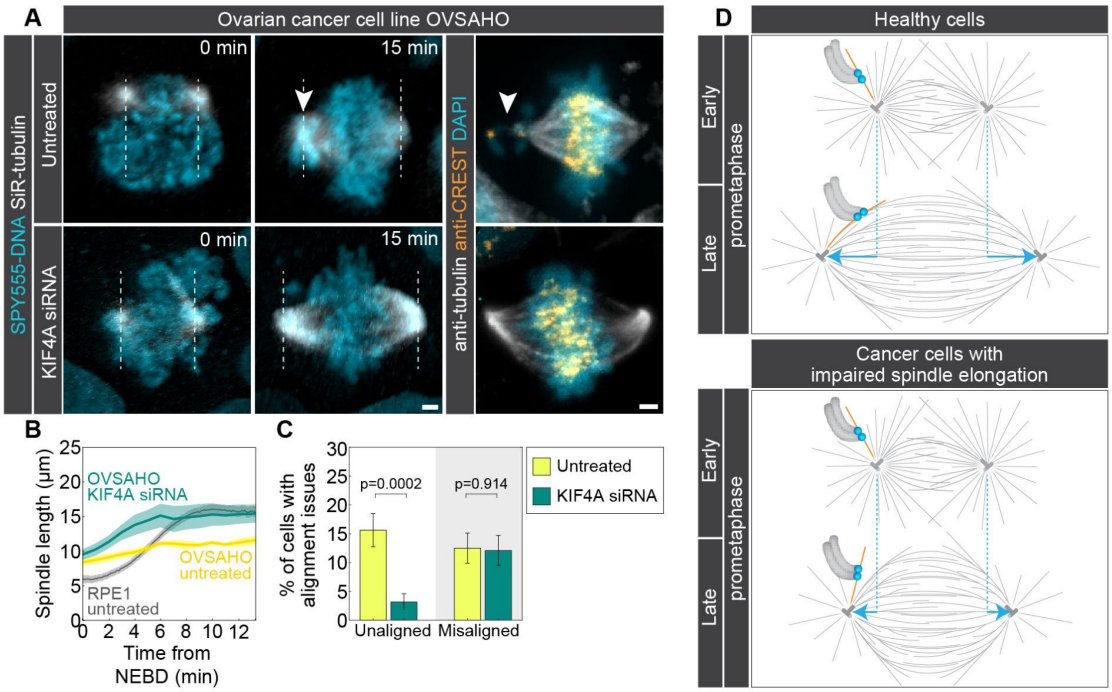

Figure 7. Robust spindle elongation prevents unaligned chromosomes. (A) Left panel: time-lapse images of control (upper) and KIF4A siRNA treated (lower) OVSAHO cells stained with SPY-555-DNA (blue) and SiR-tubulin (white) imaged using lattice light-sheet microscopy. Images show maximum intensity projections of 140 z-planes covering the whole cell, corresponding to 20.3 µm. White dashed lines represent the boundaries of polar regions. The orange arrow represents the chromosome lingering around the pole 15 minutes after NEBD. Right panel: still images of control (upper) and KIF4A siRNA treated (lower) OVSAHO cells stained with anti-α-tubulin antibody (white), anti-CREST (orange) and DAPI (blue). The orange arrow represents unaligned chromosomes in metaphase. Images are maximum intensity projections of the whole cell, covering around 15 z-planes (15 µm), depending on the size of the cell. **(B)** Spindle length in time from NEBD for control RPE1 cells (gray), control OVSAHO (orange), and KIF4A siRNA-treated OVSAHO cells (green). Values are shown as mean (dark line) and SEM (shaded areas). N = 3 untreated OVSAHO cells from 3 experiments. N = 3 KIF4A siRNA-treated OVSAHO cells from 3 experiments. N = 20 untreated RPE1 cells from 8 experiments. **(C)** Percentage of cells with alignment issues in untreated (yellow) and KIF4A siRNA-treated (green) OVSAHO cells. Alignment issues are divided into cells with unaligned (left) and misaligned (right) chromosomes. N = 160 untreated OVSAHO cells from 3 experiments. N = 157 KIF4A siRNA-treated cells OVSAHO cells from 3 experiments. Statistical test: Chi-squared test. **(D)** A model of how polar chromosomes pass across the pole in healthy cells and fail to cross the pole in cancer cells with impaired spindle elongation. In healthy cells, polar chromosomes are attached to astral microtubules. While the chromosomes remain largely immobile, the spindle elongates, thereby driving the pivoting of astral microtubules around the spindle pole. Consequently, the chromosomes with their microtubules get close to the main spindle surface, where they attach and move to the spindle midplane.

In cells with impaired spindle elongation, chromosomes are once again attached to astral microtubules and remain relatively immobile. However, the elongation is insufficient to drive microtubule pivoting from the back of the spindle all the way towards the main spindle surface, leaving polar chromosomes persistently unaligned. **(A)** Scale bars, 2 µm.

Discussion

The pivoting model

Our study uncovers how polar chromosomes, which are at highest risk of mis-segregation, get rescued from the "danger zone" behind the spindle pole. We found that spindle elongation prompts microtubules attached to polar chromosomes to pivot around the centrosome towards the spindle center, thereby enabling the contact of polar chromosomes with the spindle surface (Figure 7D).

Our findings indicate that, once the centripetal chromosome movement ends, polar chromosomes usually remain attached to the same microtubule bundle extending from the centrosome until approaching the spindle surface. If the microtubules were to extend at a constant angle from the centrosome, the chromosome would move along with the centrosome, away from the spindle center. However, instead of moving, the chromosome remains stationary, and it is the angle of the microtubules that changes, repositioning the chromosomes from behind the centrosome to its front side where it can congress to the spindle midplane.

This mechanism relies on a biomechanical property of the microtubule-centrosome connection that enables the microtubules to pivot under force. A striking example of pivoting occurred when a kinetochore fiber was pulled by a microneedle, causing the entire fiber to pivot outward around the centrosome (Suresh et al., 2022, 2020). Even though not all species possess a centrosome, the pivoting capability is conserved, as in yeast microtubules pivot around the spindle pole body, the functional equivalent of the centrosome (Kalinina et al., 2013). Whereas passive thermal pivoting in yeast promotes kinetochore capture (Blackwell et al., 2017b; Cojoc et al., 2016; Kalinina et al., 2013), active motor-driven pivoting drives spindle assembly and movement into the bud (Baumgärtner and Tolić, 2014; Blackwell et al., 2017a; Fong et al., 2021; Winters et al., 2019). Our results show that in human cells, active pivoting is driven by Eg5-powered spindle elongation, while passive pivoting occurs at non-moving centrosomes. Even though passive pivoting has a small amplitude, it may promote the initial capture of kinetochores and cortical anchors.

Structurally, the microtubule-anchoring pole component, Spc110, regulates the pivoting flexibility in yeast (Fong et al., 2021). Given that in animal cells the pericentriolar material anchors the microtubules at the centrosome (Woodruff et al., 2014), it will be interesting to explore how mechanical properties of the pericentriolar material affect microtubule pivoting and, in turn, the rescue of polar chromosomes.

The role of microtubule pivoting in spindle assembly

The pivoting of microtubules attached to polar chromosomes may also play a role in spindle assembly, potentially involving mechanisms similar to those observed in yeast for the formation of parallel and antiparallel bundles (Prelogović et al., 2019; Winters et al., 2019). Typical polar chromosomes arrive at the spindle surface with mono-lateral attachments. We propose that the microtubules in the "mono" part of the attachment represent an early kinetochore fiber, which, upon chromosome arrival to the spindle surface, becomes

incorporated into the growing spindle. Thus, kinetochore fibers of polar chromosomes start to form already when the chromosome is behind the pole, which is much earlier than previously thought.

We propose that microtubules laterally attached to the polar chromosome also integrate into the spindle, forming antiparallel overlaps with microtubules extending from the opposite side. This antiparallel bundle facilitates the formation of end-on attachments on the sister kinetochore facing the further pole by guiding the growth of new microtubules towards this kinetochore. As end-on attachments of both sister kinetochores mature and lateral attachments diminish, the previously laterally attached microtubules may turn into bridging fibers that connect sister kinetochore fibers (Kajtez et al., 2016; Simunić and Tolić, 2016). Thus, polar chromosomes bring along components of their fibers to the growing spindle.

The role of microtubule pivoting in maintaining genomic stability

Our findings show that reduced microtubule pivoting caused by slow or incomplete spindle elongation can lead to chromosome mis-segregation due to the delayed arrival of polar chromosomes to the spindle surface. This delay causes both chromatids to remain on one side of the spindle midplane during anaphase, leading to their segregation into a single daughter cell and resulting in aneuploidy. While underscoring the importance of microtubule pivoting in maintaining genomic stability, these findings also identify the biomechanical principles underlying the biased mis-segregation of chromosomes located at the nuclear periphery (Klaasen et al., 2022), as these chromosomes often end up behind the spindle pole in early mitosis.

In the context of disease, we show that insufficient spindle elongation, resulting in poor microtubule pivoting, leads to unaligned chromosomes in the high-grade serous ovarian cancer cell line OVSAHO (Figure 7D). As a proof-of-concept, we rescued these errors by increasing spindle elongation, thereby revealing the potential of altering spindle elongation to modify mitotic errors in specific cancer cells.

We speculate that the spindle-elongation driven microtubule pivoting may be relevant to explain and modify errors in chromosome alignment in certain other cancer cell lines. This idea is supported by the fact that cells without PTEN, the second most frequently mutated tumor suppressor after p53 (Li et al., 1997; Turnham et al., 2020; Yin and Shen, 2008), fail to recruit Eg5 to their spindles, resulting in both shorter spindles and misaligned chromosomes (He et al., 2016). Thus, a PTEN mutation might be one of the indicators that a particular type of cancer has unaligned chromosomes that stem from impaired spindle elongation and might be rescued by restoring PTEN function. More broadly, we propose that manipulating spindle elongation in certain cancer cells could influence mitotic errors, potentially either correcting them to maintain genome stability or worsening them to a degree that compromises cell viability.

Materials & Methods

Cell lines and plasmids

The experiments were performed using the following cell lines: human hTERT-RPE1 (hTERT-immortalized retinal pigment epithelium) cells stably expressing CENP-A-GFP and human hTERT-RPE1 (hTERT-immortalized retinal pigment epithelium) cells stably expressing CENP-A-GFP and Centrin1-GFP (Magidson et al., 2011), a gift from Alexey Khodjakov (Wadsworth Center, New York State Department of Health, Albany, NY, USA); human hTERT-RPE1 cells stably expressing CENP-A-Cerulean and Mad2-mRuby (Marcozzi and Pines, 2018), a gift from Jonathon Pines (Institute of Cancer Research, London, UK); human hTERT-RPE1 cells stably expressing tubulin-EYFP and H2B-mRFP (Holland et al., 2012), a gift from Andrew Holland (Johns Hopkins University School of Medicine, Baltimore, MD, USA); human hTERT-RPE1 cells stably expressing dCas9-GFP-3xFKBP (Truong et al., 2023), a gift from Susanne Lens (Utrecht University, Utrecht, Netherlands); human hTERT-RPE1 cells stably expressing EB3-GFP and H2B-RFP, a gift from Will Krek; unlabelled human OVSAHO cell line (JCRB Cell Bank, Tebubio, Le Perray-en-Yvelines, France); and human U2OS cells stably expressing EB3-2xGFP and CENP-A-mCherry (Kajtez et al., 2016).

The plasmids used for the experiments were: pHTN HaloTag-CENP-A (Castrogiovanni et al., 2022), a gift from Patrick Meraldi (University of Geneva, Geneva, Switzerland); psPAX2 (Addgene, No. 12260); psMD2.G (Addgene, No. 12259); pLH sgRNA Chr1-telo (Dumont et al., 2020) and pLH sgRNA Chr9-cen (Truong et al., 2023), both gifts from Susanne Lens (Utrecht University, Utrecht, Netherlands).

Cell culture

All cell lines, except an OVSAHO cell line, were cultured in Dulbecco's Modified Eagle's Medium (DMEM) containing 1 g/L D-glucose, pyruvate and L-glutamine (Gibco), supplemented with 10% (vol/vol) heat-inactivated Fetal Bovine Serum (FBS, Sigma Aldrich, St. Louis, MO, USA) and penicillin (100 IU/mL)/streptomycin (100 mg/mL) solution (Lonza, Basel, Switzerland). The OVSAHO cell line was maintained in RPMI 1640 medium containing L-glutamine and sodium bicarbonate (Sigma-Aldrich, St. Louis, MO, USA), complemented with the same supplements used in the previously described DMEM medium. All cells were kept at 37 °C and 5% CO2 in a Galaxy 170 R humidified incubator (Eppendorf, Hamburg, Germany). All cell lines have been routinely examined for mycoplasma contamination by using SPY-555-DNA (1:100 000, Spirochrome, Stein am Rhein, Switzerland) and by checking if any extracellular DNA is present. All cell lines used for experiments have been confirmed to be mycoplasma free.

RNAi treatment

Cells for RNAi transfection were seeded on 35 mm uncoated dishes with the 0.17 mm (1.5 coverslip) glass thickness (Ibidi GmbH, Gräfeling, Germany) in 1 mL of the previously described DMEM medium to reach approximately 60% confluence the following day. siRNA constructs were diluted in OPTI-MEM medium (Life Technologies, Waltham, MA, US) and RNAi treatments were performed using Lipofectamine RNAiMAX Reagent (Life Technologies, Waltham, MA, US) according to the instructions provided by the manufacturer.

The siRNA constructs and their final concentrations were: 100 nM CENP-E siRNA (L-003252-000010; Dharmacon, Lafayette, CO, USA), 100 nM Spindly/CCDC99 siRNA (L-016970-00-0010, Dharmacon, Lafayette, CO, USA), 100 nM KIF4A siRNA (sc-60888; Santa Cruz Biotechnology, Dallas, TX, USA), 100 nM Kid/KIF22 siRNA (4392420; Ambion, Austin, TX, USA). Cells were incubated for four hours with the transfection mixture followed by medium replacement into the previously described DMEM medium. All experiments were performed 24 hours after siRNA transfection.

Plasmid transfection

To transiently express CENP-A in an RPE1 cell line stably expressing tubulin-EYFP and H2B-mRFP, 5 µg of pHTN HaloTag-CENP-A plasmid was used for transfection performed on Nucleofector Kit R with the Nucleofector 2b Device (Lonza) following manufacturer's instructions. The Nucleofactor Y-001 program was used for the transfection of the RPE1 cell line. After transfection, around 500 000 cells were seeded on 35 mm uncoated dishes with the 0.17 mm (1.5 coverslip) glass thickness (Ibidi GmbH, Gräfeling, Germany) in 1 mL of the previously described DMEM medium. Transfection was performed 48 hours before imaging.

Lentivirus transduction and cell line generation

To produce lentiviruses, HEK293T cells were seeded on 10 cm Petri dishes to reach 80% confluence the next day. Plasmid constructs were diluted in OPTI-MEM medium (Life Technologies, Waltham, MA, US) and transfections were performed using Lipofectamine 3000 Transfection Reagent (Life Technologies, Waltham, MA, US) according to the manufacturer's protocol. The plasmid constructs and their final masses were as follows: 10 µg of psPAX2, 5 µg of psMD2.G, 15 µg of pLH sgRNA Chr1-telo or 15 µg of pLH sgRNA Chr9-cen. The cell medium was replaced with the previously described DMEM medium 24 hours after transfection. Lentiviruses containing sgRNA for Chr1-telo or Chr9-cen were harvested 48 hours after transfection by filtering the cell medium through 45 µm filters (No. 99745, TPP, Switzerland). RPE1 cells stably expressing dCas9-GFP-3xFKBP were seeded in 6 well plates (120 000 cells/well, Thermo Fisher Scientific, Waltham, MA, USA) the day before lentivirus transduction. Lentiviruses were added to cells together with 6 µg/ml of polybrene (TR-1003-G, Merck Milipore, Darmstadt, Germany) and incubated for 24 hours.

Treatment with inhibitors

The following Eg5 inhibitors were used on a "one cell per dish" principle: STLC (final concentration 40 µM, 164739, Sigma-Aldrich, St. Louis, MO, USA) was added approximately 30 s before landing to cause spindle shortening; FCPT (final concentration 40 µM, a gift from Timothy Mitchison) was added at the end of centripetal approaching to block the spindle elongation; monastrol (final concentration 100 µM, HY-101071A, MedChemExpress, Monmouth Junction, USA) was added 30 s before landing and then washed out with a pre-warmed DMEM medium when spindle stopped shortening. Nocodazole (final concentration 20 nM, HY-13520, MedChemExpress, Monmouth Junction, USA), Mps1 inhibitor AZ3146 (final concentration 3 µM, HY-14710, MedChemExpress, Monmouth Junction, USA), Mps1 inhibitor Cpd-5 (final concentration 62.5 nM, a gift from R. Medema via G. J. P. L. Kops lab; (Klaasen et al., 2022; Koch et al., 2016)) and actin polymerization inhibitor latrunculin A (final concentration 2 µM, 428021, Sigma-Aldrich, St. Louis, MO, USA) were added approximately 45 minutes prior to imaging and cells within the dish were subsequently imaged for 4 hours.

Live-cell dyes

To identify nuclear envelope breakdown in RPE1 cells stably expressing CENP-A-GFP and Centrin1-GFP, the SPY-555 or SPY-595 DNA probe (1: 100 000, Spirochrome, Stein am Rhein, Switzerland) was added to the cells 45 minutes to 2 hours prior to imaging. When microtubules were visualized during live-cell imaging in the same cell line, the SPY-650-tubulin probe (1:50 000, Spirochrome, Stein am Rhein, Switzerland) was added to the cells 45 minutes to 2 hours prior to imaging. For the live-cell imaging of OVSAHO cells, the SPY-555 DNA probe (1: 50 000, Spirochrome, Stein am Rhein, Switzerland) was added to the cells along with the SiR-tubulin probe (100 nM, Spirochrome, Stein am Rhein, Switzerland; (Lukinavičius et al., 2014)) 45 minutes prior to imaging. The cells were subsequently imaged for 3-4 hours. For STED live-cell imaging, the SiR-tubulin probe (100 nM, Spirochrome, Stein am Rhein, Switzerland; (Lukinavičius et al., 2014)) was added to the cells 15 minutes prior to imaging and cells were subsequently imaged for 45 minutes. To avoid efflux of the dyes, a broad-spectrum efflux pump inhibitor verapamil (Spirochrome, Stein am Rhein, Switzerland) was added at a final concentration of 1 µM to cells along with tubulin and/or DNA probes. For the live-cell imaging of RPE1 cells stably expressing EYFP-α-tubulin and H2B-mRFP, cells were incubated for 30 minutes with Janelia Fluor 635 HaloTag ligand (a final concentration of 20 nM, Promega, Madison, WI, USA) 24 hours before imaging to visualize the transiently expressed CENP-A-HaloTag.

Immunofluorescence

To determine the RNAi efficiency, RPE1 cells stably expressing CENP-A-GFP and Centrin1-GFP were grown on 35 mm uncoated dishes with the 0.17 mm (1.5 coverslip) glass thickness (Ibidi GmbH, Gräfeling, Germany) and fixed by 1 ml of ice-cold methanol for 1 minute at –20 °C, except for Spindly/CCD99 immunostaining where cells were pre-extracted with 0,2% Triton in PHEM buffer (60 mM PIPES, 10 mM EGTA, 25 mM HEPES, 4 mM MgCl2) for 1 minute and subsequently fixed with 4% pre-warmed to 37 ºC for 10 minutes. Following fixation, cells were washed three times for 5 minutes with 1 ml of PBS and permeabilized with 0.5% Triton-X-100 in PBS for 15 minutes at room temperature. To block unspecific binding, cells were incubated in 1 ml of blocking buffer (1% normal goat serum (NGS)) for 1 hour at 4 °C. Cells were then washed three times for 5 minutes with 1 ml of PBS and incubated with 250 µl of primary antibody solution overnight at 4 °C. The primary antibodies were used as follows: rabbit anti-CENP-E (1:100, C7488; Sigma-Aldrich), rabbit anti-Spindly/CCD99 (1:1000, A301_354A, Bethyl), mouse anti-KIF4A (1:100, sc-365144; Santa Cruz Biotechnology), mouse anti-Kid (1:100, sc-390640; Santa Cruz Biotechnology). After the incubation with a primary antibody, cells were washed three times for 5 minutes with 1 ml of PBS and then incubated with 250 µl of secondary antibody for 1 hour at room temperature. Alexa Fluor 594 (Abcam, ab150108 or ab150076) was used as a secondary antibody at a 1:250 dilution for CENP-E, Kif4A, and Kid staining and at a 1:1000 dilution for Spindly staining.

To image polar chromosomes in a cancer cell line, OVSAHO cells were fixed with 1 ml of 4% paraformaldehyde pre-warmed to 37 ºC for 10 minutes followed by all the previously described steps for immunostaining. The primary antibodies were used as follows: rat anti-tubulin (1:500, MA1-80017, Invitrogen) and human anti-centromere protein (1:300, 15-234, Antibodies Incorporated, CA, USA). The secondary antibodies were: donkey anti-rat Alexa Fluor 488 (1:1000, Abcam, ab150153) and goat anti-human DyLight 594 (1:500, Abcam, ab96909). DAPI (1 µg/mL) was used for chromosome visualization in all cell lines.

For STED imaging, RPE1 cells stably expressing CENP-A-GFP and RPE1 cells stably expressing CENP-A-Cerulean and Mad2-mRuby were grown on 35 mm uncoated dishes with the 0.17 mm (1.5 coverslip) glass thickness (Ibidi GmbH, Gräfeling, Germany). Cell medium was removed and 0.5% Triton in PEM buffer (0.1M PIPES, 1mM EGTA, 1mM MgCl2) was added for 15 seconds to remove the components of the cytoplasm. Following extraction, cells were fixed in 3% paraformaldehyde and 0.1% glutaraldehyde solution for 10 minutes. To reduce the background fluorescence, quenching (100 mM glycine in PBS) and reduction (0.1% sodium borohydride in PBS) solutions were added for 7 and 10 minutes, respectively. To prevent non-specific binding, cells were incubated in blocking/permeabilization buffer (2% NGS and 0.5% Triton-X-100 in PBS) for 2 hours at 4 °C. Microtubules were then stained using the rat anti-tubulin primary antibody (1:500 in blocking/permeabilization buffer, MA1-80017, Invitrogen) with a 4 °C overnight incubation. The next day, cells were washed with PBS three times for 5 minutes. After washing, the secondary antibody donkey anti-rat Alexa Fluor 594 (1:1000 in blocking/permeabilization buffer, Abcam, ab150156) or donkey anti-rat Alexa Fluor 647 (1:1000 in blocking/permeabilization buffer, Abcam, ab150155) was added and incubated for 1 hour at room temperature. DAPI (1 µg/mL) or SPY-505-DNA (1:10 000, Spirochrome, Stein am Rhein, Switzerland) was added to visualize chromosomes. The protocol was originally modified for (Štimac et al., 2022) based on the protocols from (Ponjavić et al., 2021; Zhang et al., 2020).

To analyze the position of chromosomes 1 and 9 in interphase cells, RPE1 cells stably expressing Chr1-telo-GFP or Chr9-cen-GFP were stained for tubulin and centrin-3 following the same immunostaining protocol used for STED imaging. Rabbit anti-centrin-3 primary antibody (1:1000, ab228690, Abcam) and secondary donkey anti-rabbit Alexa Fluor 647 (1:1000, Abcam, ab150075) were used for immunostaining.

Microscopy

STED microscopy of fixed cells, live-cell imaging of pivoting microtubules, live-cell imaging of EB3 comets and live-cell imaging of cells treated with Cpd-5 were performed using an Expert Line easy3D STED microscope system (Abberior Instruments, Göttingen, Germany) with the 100 x/1.4NA UPLSAPO100x oil objective (Olympus, Tokio, Japan) and an avalanche photodiode (APD) detector, as previously described (Štimac et al., 2022). The 405 nm, 488 nm, 561 nm and 647 nm laser lines were used for the excitation of Cerulean, GFP, Alexa Fluor 594/mRuby/mCherry and Alexa Fluor 647/Janelia Fluor 635/SiR-tubulin, respectively. The 775 nm laser line was used for the depletion of red and far-red lines during the STED superresolution imaging. Images were acquired using the Imspector software. The xy pixel size for fixed RPE1 cells stably expressing CENP-A-GFP was 20 nm and 20-30 focal planes were acquired with the 300 nm distance between them to cover the whole cell. The xy pixel size for fixed RPE1 cells stably expressing CENP-A-Cerulean and Mad2-mRuby was 25 nm and 1 focal plane containing the kinetochores of polar chromosomes was acquired. For live-cell STED imaging of pivoting microtubules, the xy pixel size was set to 30 nm and one focal plane was acquired every 60 seconds. For confocal live-cell imaging of pivoting microtubules in RPE1 cells on the same microscope, the xy pixel size was set to 55 nm and 3 focal planes were acquired, with the 1 µm distance between the planes and 15 seconds time intervals between different time frames. For confocal live-cell imaging of EB3 comets in RPE1 cells, the xy pixel size was set to 80 nm and 3 focal planes were acquired, with the 1 µm distance between the planes and 20 seconds time intervals between different time frames. For confocal live-cell imaging of EB3 comets in U2OS cells, the xy pixel size was set to 80 nm and one focal planes was acquired, with 1 second time intervals between different time frames. For confocal live-

cell imaging of cells treated with Cpd-5, the 488 nm laser line was used to excite the GFP, the 647 nm laser line was used to excite the SPY-650-tubulin, the xy pixel size was 80 nm and 6-7 focal planes were acquired, with 1 µm distance between the planes and 20 seconds time intervals between different time frames, as previously described (Klaasen et al., 2022).

Confocal microscopy of OVSAHO cells and RPE1 cells immunostained to check the respective RNAi efficiencies was performed using a previously described microscope setup (Buđa et al., 2017), consisting of a Bruker Opterra Multipoint Scanning Confocal Microscope (Bruker Nano Surfaces, Middleton, WI, USA), mounted on a Nikon Ti-E inverted microscope with a Nikon CFI Plan Apo VC 100 x/1.4 numerical aperture oil objective (Nikon, Tokyo, Japan). To excite DAPI, GFP, Alexa Fluor 594 or DyLight 594, a 405 nm, 488 nm and 561 nm laser lines were used, respectively. Opterra Dichroic and Barrier Filter Set 405/488/561 enabled the separation of excitation light from the emitted fluorescence. Images were acquired using the Evolve 512 Delta Electron Multiplying Charge Coupled Device (EMCCD) Camera (Photometrics, Tuscon, AZ, USA), with a camera readout mode of 20 MHz. The xy pixel size was 83 nm and the slit aperture was 22 µm. In all experiments, the whole spindle stack was imaged. The z-stacks were acquired using the unidirectional xyz scan mode with the 1 µm distance between the planes to cover the entire cell.

Confocal live cell imaging of RPE1 cells stably expressing CENP-A-GFP and Centrin1-GFP treated with STLC, FCPT, monastrol and AZ3146 was performed on a Dragonfly spinning disk confocal microscope system (Andor Technology, Belfast, UK) using the 100x/1.47 HC PL APO oil objective (Nikon, Tokyo, Japan) and Sona 4.2B-6 Back-illuminated sCMOS camera (acquisition mode set to high speed, Andor Technology) linked with iXon Life 888 EMCCD Camera (EM gain set to 208, Andor Technology). To simultaneously image two channels on two independent cameras, the 565 LP image splitter was used. Images were acquired using the Fusion software. During imaging, cells were maintained at 37°C and 5% CO2 within the heating chamber (Okolab, Pozzuoli, NA, Italy). For the excitation of GFP and SPY-650-tubulin, the 488-nm and 637-nm laser lines with corresponding filters were used, respectively. Image acquisition was done every 0.4 µm with 21 focal planes and a time interval of 10 seconds.

The Lattice Lightsheet 7 system (Carl Zeiss, Germany) was used for the live cell imaging of control RPE1 cells expressing CENP-A-GFP and Centrin1-GFP and for the imaging of cells with CENP-E, Spindly/CCD99 and Kid/KIF4A depletion, inhibition of actin polymerization or nocodazole addition. The same system was used for live-cell imaging of the OVSAHO cell line. The system includes an illumination objective lens 13.3×/0.4 (at a 30° angle to cover the glass) with a static phase element and a detection objective lens 44.83×/1.0 (at a 60° angle to cover the glass) with an Alvarez manipulator, as previously described (Vukušić and Tolić, 2023). For the live-cell imaging of RPE1 cells, the GFP was excited using the 488-nm diode laser (power output 10 Mw), with the laser power set to 2.5%, LBF 405/488/561/642 emission filter and 12 ms exposure time. The detection module consisted of a Hamamatsu ORCA-Fusion sCMOS camera. The width of the imaging area was set to 32-36 µm with the x interval of 0.3 µm. Images were acquired every 6 seconds. For the live-cell imaging of OVSAHO cells, the SPY-555-DNA was excited using the 561-nm diode laser, with the laser power set to 2.0-4.0%. SiR-tubulin was excited using the 561-nm diode laser, with the laser power set to 1.0-1.5%. The exposure time was 15-20 ms. The width of the imaging area was set to 36 µm with the x interval of 0.5 µm. Images were acquired every minute. During the imaging, cells were kept at 37 °C and at 5% CO2 in a Zeiss stage incubation chamber system (Carl Zeiss, Germany). All movies were deskewed with the ZEN 3.7 software using the „Linear Interpolation“ and „Cover Glass Transformation“ settings. Deconvolution was

performed using the „Constrained Iterative“ algorithm with automatic normalization and strength set to 4.0.

Confocal imaging of chromosomes 1 and 9 in RPE1 cells was performed on the Airyscan Zeiss LSM800 confocal laser scanning microscope with the 40x/0.95 Corr M27 objective (Carl Zeiss, Germany) and LSM 800 camera. To excite DAPI, GFP, Alexa Fluor 594 and 647, the 405 nm, 488 nm, 561 nm and 647 nm laser lines were used, respectively. Images were acquired in ZEN blue 3.5 software using the Tiles recording mode, with the 0.5 µm distance between the planes to cover the whole cells.

Image analysis

In lattice light-sheet and confocal videos, kinetochores as markers for chromosomes and centrosomes as markers for spindle poles were tracked in a z-stack using the Point Tool in Fiji/ImageJ. When the signal covered several z-planes, the central z-plane was used for tracking. Spindle length, pivoting angle (i.e., the angle between the long spindle axis and the line that connects the kinetochore midpoint with the closer centrosome), cTilt (i.e., the angle between the long spindle axis and the line that connects sister kinetochores; (Renda et al., 2022)), interkinetochore distance, distance to closer and further centrosome and distance to centrosome midpoint were subsequently calculated from the coordinates in 3D using a home-written MatLab script. The end of centripetal movement was determined as a time point when the distance of the kinetochore midpoint to the closer centrosome started varying instead of continuously becoming smaller. The landing on the main spindle surface was determined as a time point when the pivoting angle was below 60° and cTilt was below 22.5° (Renda et al., 2022), symbolizing a moment when kinetochores first align along the microtubules of the main spindle surface, even if they experience subsequent detachments. The landing was additionally checked using visual inspection. The alignment was defined as the moment when the kinetochore pair was equidistant (±1-2 µm) to both poles. The formation of the prometaphase ring was visually determined as a time point when most kinetochores finish their centripetal movement. The end of spindle elongation was defined as a time point when spindle length starts varying and/or decreasing instead of continuously increasing. The anaphase onset was visually determined as a time point when sister kinetochores first start separating. Polar chromosomes were defined as those that had a pivoting angle of >90° at NEBD and subsequently made their first contact with the spindle behind the spindle pole. The position of the first contact was determined at the end of centripetal movement, when the distance of the kinetochore pair to the spindle contour was usually < 3 µm. Pivoting was then analyzed between the end of centripetal movement until after landing. In Eg5-based manipulation experiments, analysis was taken into account from the first frame when the inhibitor started working, i.e., when the spindle length started increasing or decreasing.

Successful passage across the pole was defined as the passage across the 90° mark within 15 minutes from NEBD, not taking into account any subsequent failures to form stable attachments to microtubules of the main spindle surface. Misaligned chromosomes were defined as those located within the two spindle poles and less than 2 µm away from the centrosome/spindle pole in metaphase. Unaligned chromosomes were defined as those located behind the spindle pole or, alternatively, in front of the pole but not attached to microtubules of the main spindle surface in metaphase. Lagging chromosomes were defined as those located in the central part of the spindle with a stretched kinetochore during anaphase.

When chromosomes were labeled instead of kinetochores, two points were put in the centromeric region during the tracking, with arm length measured from the centromeric region

(closest to the pole) until the end of the most visible and isolated arm. When poles were marked with tubulin or EB3 instead of Centrin1, the point was put in the center of tubulin/EB3 signal. When astral microtubules were tracked instead of chromosomes or kinetochores, their movement was tracked by putting two points along the central part of the microtubule contour and their shape was determined by putting two points at the spindle poles and subsequent five along the entire microtubule contour. Kinetochore switching between microtubules was investigated using visual analysis.

The length of long xy-, short xy- and z nuclear axes was measured on maximum intensity projections of the whole cell just before NEBD using the Line Tool in ImageJ. The long xy axis was defined as the axis with the largest distance between the two opposite sides of the nuclear border, the short xy axis was defined as perpendicular to the middle of the long xy axis and z axis was defined as the distance from the first focal plane in which the signal was present until the last. The spindle axis, used to determine the danger zone, was measured using the Line Tool in ImageJ on maximum intensity projections of the whole cell when the prometaphase ring formed and most kinetochores finished their centripetal movement. The angle between the long nuclear xy axis just before NEBD and the long spindle axis in prometaphase was then calculated to determine which chromosomes are most likely to attach behind the pole. This angle was also compared to the angle between the long cellular xy axis at NEBD, determined using the Line Tool in ImageJ, and the long spindle axis in prometaphase.

The long axis of interphase RPE1 dCas9-GFP cells with labeled subtelomeric region of chromosome 1 or pericentromeric region of chromosome 9 was measured on maximum intensity projections of the whole cell. The long axis was then divided into three equal parts that represent the borders of three cellular compartments - two polar zones and the central zone. The position of the labeled chromosomes was determined as polar if they were located in any of the polar zones and as central if they were located in the central zone, respectively.

To determine the position of kinetochore pairs relative to the pole in STED images, kinetochores and poles were marked in 3D using a Point Tool in ImageJ and the angle that the line connecting the kinetochore pair midpoint with the closer centrosome forms with the long spindle axis (i.e., pivoting angle) was subsequently calculated using a home-written MatLab script. Kinetochore pairs in these images were considered polar if they were located above 90° or, alternatively, were located around the pole but not attached to the microtubules of the main spindle surface during later stages of prometaphase.

Polar chromosomes were considered as attached to microtubules when there was a microtubule either directly ending at the kinetochore or in very close proximity to the kinetochore. Polar chromosomes were considered unattached when there was no microtubule in their proximity. The type of attachment was determined using visual inspection. Additionally, for cells with labeled Mad2 and CENP-A, Mad2 and CENP-A levels were measured using the Polygon Tool in ImageJ. The same polygon was used for measuring the signal in both channels for the same kinetochore, as well as for the background in both channels. The final Mad2/CENP-A signal on the kinetochore was calculated using the formula: Mad2/CENP-A signal = (Integrated density of Mad2 on the kinetochore – (Kinetochore area x Mean fluorescence of the background))/(Integrated density of CENP-A on the kinetochore – (Kinetochore area x Mean fluorescence of the background)).

The intensity of microtubules from the opposite side of the spindle, the intensity of astral microtubules and the accompanying background were measured in a single z-plane using the 20x20 pixel Square Tool in ImageJ. The final intensity of the microtubules was then calculated using the formula: Microtubule intensity = Mean intensity of the microtubule – Mean intensity of the background.

CENP-E, Spindly, KIF4A and Kid intensities were measured in sum intensity projections of the entire cell, covering 33 z-planes or 33 µm. The total signal of the protein of interest within the spindle was marked by using the Polygon Tool in ImageJ. Background in the cytoplasm was measured using the 25x25 pixel Square Tool. The total intensities were calculated using the following formula: Protein intensity = Integrated density within the spindle – (Area of the spindle x Mean fluorescence of the background). The total intensities were then normalized to the mean total intensity obtained from control cells.

All measurements were performed in ImageJ/Fiji (National Institutes of Health), followed by data analysis in MATLAB (MathWorks). Figures and schematic representations were assembled in Adobe Illustrator CC (Adobe Systems). Statistical analysis was performed as noted in the respective Figure captions.

Author Contribution

I.K. and V.Š. performed all experiments and analyzed the data, except the experiments and analyses on chromosome 1 and 9, which were performed by P.M. I.K., V.Š., and I.M.T. wrote the manuscript. I.M.T. supervised the project.

Acknowledgments

The authors thank Alexey Khodjakov, Jonathon Pines, Andrew Holland, Will Krek, Susanne Lens and Julie Welburn for the cell lines; Oliver Vugrek and Filip Rokić for help with lentiviral work, Marko Šprem and the Abberior team for help with the Expert Line easy3D STED microscope system setup and developing microscopy protocols; Ivana Šarić for help with the drawings, members of the Tolić, Pavin and Kops groups for helpful discussions and advice. The authors acknowledge funding by the European Research Council (ERC Synergy Grant, GA Number 855158), the Croatian Science Foundation (HRZZ) through Swiss-Croatian Bilateral Projects (project IPCH-2022-10-9344) and Cooperation Programme with Croatian Scientists in the Diaspora "Research Cooperability" (project PZS-2019-02-7653), and projects co-financed by the Croatian Government and the European Union through the European Regional Development Fund—the Competitiveness and Cohesion Operational Programme: IPSted (Grant KK.01.1.1.04.0057) and QuantiXLie Center of Excellence (Grant KK.01.1.1.01.0004).

References

Alexander, S.P., Rieder, C.L., 1991. Chromosome motion during attachment to the vertebrate spindle: initial saltatory-like behavior of chromosomes and quantitative analysis of force production by nascent kinetochore fibers. J Cell Biol 113, 805–815. https://doi.org/10.1083/jcb.113.4.805

Barisic, M., Aguiar, P., Geley, S., Maiato, H., 2014. Kinetochore motors drive congression of peripheral polar chromosomes by overcoming random arm-ejection forces. Nat Cell Biol 16, 1249–1256. https://doi.org/10.1038/ncb3060

Barretina, J., Caponigro, G., Stransky, N., Venkatesan, K., Margolin, A.A., Kim, S., Wilson, C.J., Lehár, J., Kryukov, G.V., Sonkin, D., Reddy, A., Liu, M., Murray, L., Berger, M.F., Monahan, J.E., Morais, P., Meltzer, J., Korejwa, A., Jané-Valbuena, J., Mapa,

F.A., Thibault, J., Bric-Furlong, E., Raman, P., Shipway, A., Engels, I.H., Cheng, J., Yu, G.K., Yu, J., Aspesi, P., de Silva, M., Jagtap, K., Jones, M.D., Wang, L., Hatton, C., Palescandolo, E., Gupta, S., Mahan, S., Sougnez, C., Onofrio, R.C., Liefeld, T., MacConaill, L., Winckler, W., Reich, M., Li, N., Mesirov, J.P., Gabriel, S.B., Getz, G., Ardlie, K., Chan, V., Myer, V.E., Weber, B.L., Porter, J., Warmuth, M., Finan, P., Harris, J.L., Meyerson, M., Golub, T.R., Morrissey, M.P., Sellers, W.R., Schlegel, R., Garraway, L.A., 2012. The Cancer Cell Line Encyclopedia enables predictive modelling of anticancer drug sensitivity. Nature 483, 603–607. https://doi.org/10.1038/nature11003

Baumgärtner, S., Tolić, I.M., 2014. Astral microtubule pivoting promotes their search for cortical anchor sites during mitosis in budding yeast. PLoS One 9, e93781. https://doi.org/10.1371/journal.pone.0093781

Berg, H.C., 1993. Random Walks in Biology. Princeton Univ. Press.

Bird, A.W., Hyman, A.A., 2008. Building a spindle of the correct length in human cells requires the interaction between TPX2 and Aurora A. J Cell Biol 182, 289–300. https://doi.org/10.1083/jcb.200802005

Blackwell, R., Edelmaier, C., Sweezy-Schindler, O., Lamson, A., Gergely, Z.R., O'Toole, E., Crapo, A., Hough, L.E., McIntosh, J.R., Glaser, M.A., Betterton, M.D., 2017a. Physical determinants of bipolar mitotic spindle assembly and stability in fission yeast. Sci Adv 3, e1601603. https://doi.org/10.1126/sciadv.1601603

Blackwell, R., Sweezy-Schindler, O., Edelmaier, C., Gergely, Z.R., Flynn, P.J., Montes, S., Crapo, A., Doostan, A., McIntosh, J.R., Glaser, M.A., Betterton, M.D., 2017b. Contributions of Microtubule Dynamic Instability and Rotational Diffusion to Kinetochore Capture. Biophys J 112, 552–563. https://doi.org/10.1016/j.bpj.2016.09.006

Bolzer, A., Kreth, G., Solovei, I., Koehler, D., Saracoglu, K., Fauth, C., Müller, S., Eils, R., Cremer, C., Speicher, M.R., Cremer, T., 2005. Three-Dimensional Maps of All Chromosomes in Human Male Fibroblast Nuclei and Prometaphase Rosettes. PLOS Biology 3, e157. https://doi.org/10.1371/journal.pbio.0030157

Booth, A.J., Yue, Z., Eykelenboom, J.K., Stiff, T., Luxton, G.G., Hochegger, H., Tanaka, T.U., 2019. Contractile acto-myosin network on nuclear envelope remnants positions human chromosomes for mitosis. eLife 8, e46902. https://doi.org/10.7554/eLife.46902

Buđa, R., Vukušić, K., Tolić, I.M., 2017. Dissection and characterization of microtubule bundles in the mitotic spindle using femtosecond laser ablation, in: Lecuit, T. (Ed.), Methods in Cell Biology, Cell Polarity and Morphogenesis. Academic Press, pp. 81–101. https://doi.org/10.1016/bs.mcb.2016.11.007

Cai, S., O'Connell, C.B., Khodjakov, A., Walczak, C.E., 2009. Chromosome congression in the absence of kinetochore fibres. Nat Cell Biol 11, 832–838. https://doi.org/10.1038/ncb1890

Castrogiovanni, C., Inchingolo, A.V., Harrison, J.U., Dudka, D., Sen, O., Burroughs, N.J., McAinsh, A.D., Meraldi, P., 2022. Evidence for a HURP/EB free mixed-nucleotide zone in kinetochore-microtubules. Nat Commun 13, 4704. https://doi.org/10.1038/s41467-022-32421-x

Cerami, E., Gao, J., Dogrusoz, U., Gross, B.E., Sumer, S.O., Aksoy, B.A., Jacobsen, A.,

Byrne, C.J., Heuer, M.L., Larsson, E., Antipin, Y., Reva, B., Goldberg, A.P., Sander, C., Schultz, N., 2012. The cBio cancer genomics portal: an open platform for exploring multidimensional cancer genomics data. Cancer Discov 2, 401–404. https://doi.org/10.1158/2159-8290.CD-12-0095

Chong, M.K., Rosas-Salvans, M., Tran, V., Dumont, S., 2024. Chromosome size-dependent polar ejection force impairs mammalian mitotic error correction. J Cell Biol 223, e202310010. https://doi.org/10.1083/jcb.202310010

Cojoc, G., Florescu, A.-M., Krull, A., Klemm, A.H., Pavin, N., Jülicher, F., Tolić, I.M., 2016. Paired arrangement of kinetochores together with microtubule pivoting and dynamics drive kinetochore capture in meiosis I. Sci Rep 6, 25736. https://doi.org/10.1038/srep25736

Craske, B., Welburn, J.P.I., 2020. Leaving no-one behind: how CENP-E facilitates chromosome alignment. Essays Biochem 64, 313–324. https://doi.org/10.1042/EBC20190073

de Bruijn, I., Kundra, R., Mastrogiacomo, B., Tran, T.N., Sikina, L., Mazor, T., Li, X., Ochoa, A., Zhao, G., Lai, B., Abeshouse, A., Baiceanu, D., Ciftci, E., Dogrusoz, U., Dufilie, A., Erkoc, Z., Garcia Lara, E., Fu, Z., Gross, B., Haynes, C., Heath, A., Higgins, D., Jagannathan, P., Kalletla, K., Kumari, P., Lindsay, J., Lisman, A., Leenknegt, B., Lukasse, P., Madela, D., Madupuri, R., van Nierop, P., Plantalech, O., Quach, J., Resnick, A.C., Rodenburg, S.Y.A., Satravada, B.A., Schaeffer, F., Sheridan, R., Singh, J., Sirohi, R., Sumer, S.O., van Hagen, S., Wang, A., Wilson, M., Zhang, H., Zhu, K., Rusk, N., Brown, S., Lavery, J.A., Panageas, K.S., Rudolph, J.E., LeNoue-Newton, M.L., Warner, J.L., Guo, X., Hunter-Zinck, H., Yu, T.V., Pilai, S., Nichols, C., Gardos, S.M., Philip, J., AACR Project GENIE BPC Core Team, AACR Project GENIE Consortium, Kehl, K.L., Riely, G.J., Schrag, D., Lee, J., Fiandalo, M.V., Sweeney, S.M., Pugh, T.J., Sander, C., Cerami, E., Gao, J., Schultz, N., 2023. Analysis and Visualization of Longitudinal Genomic and Clinical Data from the AACR Project GENIE Biopharma Collaborative in cBioPortal. Cancer Res 83, 3861–3867. https://doi.org/10.1158/0008-5472.CAN-23-0816

Dick, A.E., Gerlich, D.W., 2013. Kinetic framework of spindle assembly checkpoint signalling. Nat Cell Biol 15, 1370–1377. https://doi.org/10.1038/ncb2842

Dumont, M., Gamba, R., Gestraud, P., Klaasen, S., Worrall, J.T., De Vries, S.G., Boudreau, V., Salinas-Luypaert, C., Maddox, P.S., Lens, S.M., Kops, G.J., McClelland, S.E., Miga, K.H., Fachinetti, D., 2020. Human chromosome-specific aneuploidy is influenced by DNA-dependent centromeric features. EMBO J 39, e102924. https://doi.org/10.15252/embj.2019102924

Ertych, N., Stolz, A., Stenzinger, A., Weichert, W., Kaulfuß, S., Burfeind, P., Aigner, A., Wordeman, L., Bastians, H., 2014. Increased microtubule assembly rates influence chromosomal instability in colorectal cancer cells. Nat Cell Biol 16, 779–791. https://doi.org/10.1038/ncb2994

Ferrandiz, N., Downie, L., Starling, G.P., Royle, S.J., 2022. Endomembranes promote chromosome missegregation by ensheathing misaligned chromosomes. J Cell Biol 221, e202203021. https://doi.org/10.1083/jcb.202203021

Fong, K.K., Davis, T.N., Asbury, C.L., 2021. Microtubule pivoting enables mitotic spindle assembly in *S. cerevisiae*. Journal of Cell Biology 220, e202007193. https://doi.org/10.1083/jcb.202007193

Gao, J., Aksoy, B.A., Dogrusoz, U., Dresdner, G., Gross, B., Sumer, S.O., Sun, Y., Jacobsen, A., Sinha, R., Larsson, E., Cerami, E., Sander, C., Schultz, N., 2013. Integrative analysis of complex cancer genomics and clinical profiles using the cBioPortal. Sci Signal 6, pl1. https://doi.org/10.1126/scisignal.2004088

Ghandi, M., Huang, F.W., Jané-Valbuena, J., Kryukov, G.V., Lo, C.C., McDonald, E.R., Barretina, J., Gelfand, E.T., Bielski, C.M., Li, H., Hu, K., Andreev-Drakhlin, A.Y., Kim, J., Hess, J.M., Haas, B.J., Aguet, F., Weir, B.A., Rothberg, M.V., Paolella, B.R., Lawrence, M.S., Akbani, R., Lu, Y., Tiv, H.L., Gokhale, P.C., de Weck, A., Mansour, A.A., Oh, C., Shih, J., Hadi, K., Rosen, Y., Bistline, J., Venkatesan, K., Reddy, A., Sonkin, D., Liu, M., Lehar, J., Korn, J.M., Porter, D.A., Jones, M.D., Golji, J., Caponigro, G., Taylor, J.E., Dunning, C.M., Creech, A.L., Warren, A.C., McFarland, J.M., Zamanighomi, M., Kauffmann, A., Stransky, N., Imielinski, M., Maruvka, Y.E., Cherniack, A.D., Tsherniak, A., Vazquez, F., Jaffe, J.D., Lane, A.A., Weinstock, D.M., Johannessen, C.M., Morrissey, M.P., Stegmeier, F., Schlegel, R., Hahn, W.C., Getz, G., Mills, G.B., Boehm, J.S., Golub, T.R., Garraway, L.A., Sellers, W.R., 2019. Next-generation characterization of the Cancer Cell Line Encyclopedia. Nature 569, 503–508. https://doi.org/10.1038/s41586-019-1186-3

Girish, V., Lakhani, A.A., Thompson, S.L., Scaduto, C.M., Brown, L.M., Hagenson, R.A., Sausville, E.L., Mendelson, B.E., Kandikuppa, P.K., Lukow, D.A., Yuan, M.L., Stevens, E.C., Lee, S.N., Schukken, K.M., Akalu, S.M., Vasudevan, A., Zou, C., Salovska, B., Li, W., Smith, J.C., Taylor, A.M., Martienssen, R.A., Liu, Y., Sun, R., Sheltzer, J.M., 2023. Oncogene-like addiction to aneuploidy in human cancers. Science 381, eadg4521. https://doi.org/10.1126/science.adg4521

Gliech, C.R., Yeow, Z.Y., Tapias-Gomez, D., Yang, Y., Huang, Z., Tijhuis, A.E., Spierings, D.C., Foijer, F., Chung, G., Tamayo, N., Bahrami-Nejad, Z., Collins, P., Nguyen, T.T., Plata Stapper, A., Hughes, P.E., Payton, M., Holland, A.J., 2024. Weakened APC/C activity at mitotic exit drives cancer vulnerability to KIF18A inhibition. EMBO J 43, 666–694. https://doi.org/10.1038/s44318-024-00031-6

Gomes, A.M., Orr, B., Novais-Cruz, M., De Sousa, F., Macário-Monteiro, J., Lemos, C., Ferrás, C., Maiato, H., 2022. Micronuclei from misaligned chromosomes that satisfy the spindle assembly checkpoint in cancer cells. Curr Biol 32, 4240-4254.e5. https://doi.org/10.1016/j.cub.2022.08.026

Griffis, E.R., Stuurman, N., Vale, R.D., 2007. Spindly, a novel protein essential for silencing the spindle assembly checkpoint, recruits dynein to the kinetochore. J Cell Biol 177, 1005–1015. https://doi.org/10.1083/jcb.200702062

Groen, A.C., Needleman, D., Brangwynne, C., Gradinaru, C., Fowler, B., Mazitschek, R., Mitchison, T.J., 2008. A novel small-molecule inhibitor reveals a possible role of kinesin-5 in anastral spindle-pole assembly. J Cell Sci 121, 2293–2300. https://doi.org/10.1242/jcs.024018

He, J., Zhang, Z., Ouyang, M., Yang, F., Hao, H., Lamb, K.L., Yang, J., Yin, Y., Shen, W.H., 2016. PTEN regulates EG5 to control spindle architecture and chromosome congression during mitosis. Nat Commun 7, 12355. https://doi.org/10.1038/ncomms12355

Hewitt, L., Tighe, A., Santaguida, S., White, A.M., Jones, C.D., Musacchio, A., Green, S., Taylor, S.S., 2010. Sustained Mps1 activity is required in mitosis to recruit O-Mad2 to the Mad1-C-Mad2 core complex. J Cell Biol 190, 25–34. https://doi.org/10.1083/jcb.201002133

Holland, A.J., Fachinetti, D., Da Cruz, S., Zhu, Q., Vitre, B., Lince-Faria, M., Chen, D., Parish, N., Verma, I.M., Bettencourt-Dias, M., Cleveland, D.W., 2012. Polo-like kinase 4 controls centriole duplication but does not directly regulate cytokinesis. Mol Biol Cell 23, 1838–1845. https://doi.org/10.1091/mbc.E11-12-1043

Jagrić, M., Risteski, P., Martinčić, J., Milas, A., Tolić, I.M., 2021. Optogenetic control of PRC1 reveals its role in chromosome alignment on the spindle by overlap length-dependent forces. eLife 10, e61170. https://doi.org/10.7554/eLife.61170

Kabeche, L., Compton, D.A., 2013. Cyclin A regulates kinetochore microtubules to promote faithful chromosome segregation. Nature 502, 110–113. https://doi.org/10.1038/nature12507

Kajtez, J., Solomatina, A., Novak, M., Polak, B., Vukušić, K., Rüdiger, J., Cojoc, G., Milas, A., Šumanovac Šestak, I., Risteski, P., Tavano, F., Klemm, A.H., Roscioli, E., Welburn, J., Cimini, D., Glunčić, M., Pavin, N., Tolić, I.M., 2016. Overlap microtubules link sister k-fibres and balance the forces on bi-oriented kinetochores. Nat Commun 7, 10298. https://doi.org/10.1038/ncomms10298

Kalinina, I., Nandi, A., Delivani, P., Chacón, M.R., Klemm, A.H., Ramunno-Johnson, D., Krull, A., Lindner, B., Pavin, N., Tolić-Nørrelykke, I.M., 2013. Pivoting of microtubules around the spindle pole accelerates kinetochore capture. Nat Cell Biol 15, 82–87. https://doi.org/10.1038/ncb2640

Kapitein, L.C., Peterman, E.J.G., Kwok, B.H., Kim, J.H., Kapoor, T.M., Schmidt, C.F., 2005. The bipolar mitotic kinesin Eg5 moves on both microtubules that it crosslinks. Nature 435, 114–118. https://doi.org/10.1038/nature03503

Kapoor, T.M., Lampson, M.A., Hergert, P., Cameron, L., Cimini, D., Salmon, E.D., McEwen, B.F., Khodjakov, A., 2006. Chromosomes Can Congress to the Metaphase Plate Before Biorientation. Science 311, 388–391. https://doi.org/10.1126/science.1122142

Kashina, A.S., Rogers, G.C., Scholey, J.M., 1997. The bimC family of kinesins: essential bipolar mitotic motors driving centrosome separation. Biochim Biophys Acta 1357, 257–271. https://doi.org/10.1016/s0167-4889(97)00037-2

Klaasen, S.J., Truong, M.A., van Jaarsveld, R.H., Koprivec, I., Štimac, V., de Vries, S.G., Risteski, P., Kodba, S., Vukušić, K., de Luca, K.L., Marques, J.F., Gerrits, E.M., Bakker, B., Foijer, F., Kind, J., Tolić, I.M., Lens, S.M.A., Kops, G.J.P.L., 2022. Nuclear chromosome locations dictate segregation error frequencies. Nature 607, 604–609. https://doi.org/10.1038/s41586-022-04938-0

Kletter, T., Reusch, S., Cavazza, T., Dempewolf, N., Tischer, C., Reber, S., 2021. Volumetric morphometry reveals spindle width as the best predictor of mammalian spindle scaling. J Cell Biol 221, e202106170. https://doi.org/10.1083/jcb.202106170

Koch, A., Maia, A., Janssen, A., Medema, R.H., 2016. Molecular basis underlying resistance to Mps1/TTK inhibitors. Oncogene 35, 2518–2528. https://doi.org/10.1038/onc.2015.319

Kuhn, J., Dumont, S., 2017. Spindle assembly checkpoint satisfaction occurs via end-on but not lateral attachments under tension. Journal of Cell Biology 216, 1533–1542. https://doi.org/10.1083/jcb.201611104

Li, J., Yen, C., Liaw, D., Podsypanina, K., Bose, S., Wang, S.I., Puc, J., Miliaresis, C., Rodgers, L., McCombie, R., Bigner, S.H., Giovanella, B.C., Ittmann, M., Tycko, B.,

Hibshoosh, H., Wigler, M.H., Parsons, R., 1997. PTEN, a putative protein tyrosine phosphatase gene mutated in human brain, breast, and prostate cancer. Science 275, 1943–1947. https://doi.org/10.1126/science.275.5308.1943

Li, Y., Yu, W., Liang, Y., Zhu, X., 2007. Kinetochore dynein generates a poleward pulling force to facilitate congression and full chromosome alignment. Cell Res 17, 701–712. https://doi.org/10.1038/cr.2007.65

Lukinavičius, G., Reymond, L., D'Este, E., Masharina, A., Göttfert, F., Ta, H., Güther, A., Fournier, M., Rizzo, S., Waldmann, H., Blaukopf, C., Sommer, C., Gerlich, D.W., Arndt, H.-D., Hell, S.W., Johnsson, K., 2014. Fluorogenic probes for live-cell imaging of the cytoskeleton. Nat Methods 11, 731–733. https://doi.org/10.1038/nmeth.2972

Magidson, V., O'Connell, C.B., Lončarek, J., Paul, R., Mogilner, A., Khodjakov, A., 2011. The spatial arrangement of chromosomes during prometaphase facilitates spindle assembly. Cell 146, 555–567. https://doi.org/10.1016/j.cell.2011.07.012

Maiato, H., Gomes, A.M., Sousa, F., Barisic, M., 2017. Mechanisms of Chromosome Congression during Mitosis. Biology (Basel) 6, 13. https://doi.org/10.3390/biology6010013

Marcozzi, C., Pines, J., 2018. Chapter 1 - Assays for the spindle assembly checkpoint in cell culture, in: Maiato, H., Schuh, M. (Eds.), Methods in Cell Biology, Mitosis and Meiosis Part A. Academic Press, pp. 1–13. https://doi.org/10.1016/bs.mcb.2018.03.001

Mayer, T.U., Kapoor, T.M., Haggarty, S.J., King, R.W., Schreiber, S.L., Mitchison, T.J., 1999. Small molecule inhibitor of mitotic spindle bipolarity identified in a phenotype-based screen. Science 286, 971–974. https://doi.org/10.1126/science.286.5441.971

Mazumdar, M., Sundareshan, S., Misteli, T., 2004. Human chromokinesin KIF4A functions in chromosome condensation and segregation. J Cell Biol 166, 613–620. https://doi.org/10.1083/jcb.200401142

McEwen, B.F., Chan, G.K., Zubrowski, B., Savoian, M.S., Sauer, M.T., Yen, T.J., 2001. CENP-E is essential for reliable bioriented spindle attachment, but chromosome alignment can be achieved via redundant mechanisms in mammalian cells. Mol Biol Cell 12, 2776–2789. https://doi.org/10.1091/mbc.12.9.2776

Novais-Cruz, M., Pombinho, A., Sousa, M., Maia, A.F., Maiato, H., Ferrás, C., 2023. Mitotic DNA damage promotes chromokinesin-mediated missegregation of polar chromosomes in cancer cells. Mol Biol Cell 34, ar47. https://doi.org/10.1091/mbc.E22-11-0518

Pereira, C., Reis, R.M., Gama, J.B., Celestino, R., Cheerambathur, D.K., Carvalho, A.X., Gassmann, R., 2018. Self-Assembly of the RZZ Complex into Filaments Drives Kinetochore Expansion in the Absence of Microtubule Attachment. Curr Biol 28, 3408-3421.e8. https://doi.org/10.1016/j.cub.2018.08.056

Plessner, M., Knerr, J., Grosse, R., 2019. Centrosomal Actin Assembly Is Required for Proper Mitotic Spindle Formation and Chromosome Congression. iScience 15, 274–281. https://doi.org/10.1016/j.isci.2019.04.022

Ponjavić, I., Vukušić, K., Tolić, I.M., 2021. Expansion microscopy of the mitotic spindle. Methods Cell Biol 161, 247–274. https://doi.org/10.1016/bs.mcb.2020.04.014

Prelogović, M., Winters, L., Milas, A., Tolić, I.M., Pavin, N., 2019. Pivot-and-bond model explains microtubule bundle formation. Phys. Rev. E 100, 012403. https://doi.org/10.1103/PhysRevE.100.012403

Rajendraprasad, G., Eibes, S., Boldú, C.G., Barisic, M., 2021. TH588 and Low-Dose Nocodazole Impair Chromosome Congression by Suppressing Microtubule Turnover within the Mitotic Spindle. Cancers 13, 5995. https://doi.org/10.3390/cancers13235995

Reinhold, W.C., Sunshine, M., Liu, H., Varma, S., Kohn, K.W., Morris, J., Doroshow, J., Pommier, Y., 2012. CellMiner: a web-based suite of genomic and pharmacologic tools to explore transcript and drug patterns in the NCI-60 cell line set. Cancer Res 72, 3499–3511. https://doi.org/10.1158/0008-5472.CAN-12-1370

Renda, F., Miles, C., Tikhonenko, I., Fisher, R., Carlini, L., Kapoor, T.M., Mogilner, A., Khodjakov, A., 2022. Non-centrosomal microtubules at kinetochores promote rapid chromosome biorientation during mitosis in human cells. Current Biology S0960982222000240. https://doi.org/10.1016/j.cub.2022.01.013

Rickert, K.W., Schaber, M., Torrent, M., Neilson, L.A., Tasber, E.S., Garbaccio, R., Coleman, P.J., Harvey, D., Zhang, Y., Yang, Y., Marshall, G., Lee, L., Walsh, E.S., Hamilton, K., Buser, C.A., 2008. Discovery and biochemical characterization of selective ATP competitive inhibitors of the human mitotic kinesin KSP. Arch Biochem Biophys 469, 220–231. https://doi.org/10.1016/j.abb.2007.10.016

Rieder, C.L., Alexander, S.P., 1990. Kinetochores are transported poleward along a single astral microtubule during chromosome attachment to the spindle in newt lung cells. J Cell Biol 110, 81–95. https://doi.org/10.1083/jcb.110.1.81

Risteski, P., Božan, D., Jagrić, M., Bosilj, A., Pavin, N., Tolić, I.M., 2022. Length-dependent poleward flux of sister kinetochore fibers promotes chromosome alignment. Cell Rep 40, 111169. https://doi.org/10.1016/j.celrep.2022.111169

Risteski, P., Martinčić, J., Tintor, E., Jagrić, M., Tolić, I.M., 2024. Microtubule poleward flux as a target for modifying chromosome segregation errors. bioRxiv 2024.03.11.584498. https://doi.org/10.1101/2024.03.11.584498

Sacristan, C., Ahmad, M.U.D., Keller, J., Fermie, J., Groenewold, V., Tromer, E., Fish, A., Melero, R., Carazo, J.M., Klumperman, J., Musacchio, A., Perrakis, A., Kops, G.J., 2018. Dynamic kinetochore size regulation promotes microtubule capture and chromosome biorientation in mitosis. Nat Cell Biol 20, 800–810. https://doi.org/10.1038/s41556-018-0130-3

Shrestha, R.L., Draviam, V.M., 2013. Lateral to end-on conversion of chromosome-microtubule attachment requires kinesins CENP-E and MCAK. Curr Biol 23, 1514–1526. https://doi.org/10.1016/j.cub.2013.06.040

Simunić, J., Tolić, I.M., 2016. Mitotic Spindle Assembly: Building the Bridge between Sister K-Fibers. Trends in Biochemical Sciences 41, 824–833. https://doi.org/10.1016/j.tibs.2016.07.004

Skoufias, D.A., DeBonis, S., Saoudi, Y., Lebeau, L., Crevel, I., Cross, R., Wade, R.H., Hackney, D., Kozielski, F., 2006. S-trityl-L-cysteine is a reversible, tight binding inhibitor of the human kinesin Eg5 that specifically blocks mitotic progression. J Biol Chem 281, 17559–17569. https://doi.org/10.1074/jbc.M511735200

Stepanova, T., Slemmer, J., Hoogenraad, C.C., Lansbergen, G., Dortland, B., De Zeeuw, C.I.,

Grosveld, F., van Cappellen, G., Akhmanova, A., Galjart, N., 2003. Visualization of Microtubule Growth in Cultured Neurons via the Use of EB3-GFP (End-Binding Protein 3-Green Fluorescent Protein). J Neurosci 23, 2655–2664. https://doi.org/10.1523/JNEUROSCI.23-07-02655.2003

Stiff, T., Echegaray-Iturra, F.R., Pink, H.J., Herbert, A., Reyes-Aldasoro, C.C., Hochegger, H., 2020. Prophase-Specific Perinuclear Actin Coordinates Centrosome Separation and Positioning to Ensure Accurate Chromosome Segregation. Cell Reports 31. https://doi.org/10.1016/j.celrep.2020.107681

Štimac, V., Koprivec, I., Manenica, M., Simunić, J., Tolić, I.M., 2022. Augmin prevents merotelic attachments by promoting proper arrangement of bridging and kinetochore fibers. eLife 11, e83287. https://doi.org/10.7554/eLife.83287

Suresh, P., Galstyan, V., Phillips, R., Dumont, S., 2022. Modeling and mechanical perturbations reveal how spatially regulated anchorage gives rise to spatially distinct mechanics across the mammalian spindle. Elife 11, e79558. https://doi.org/10.7554/eLife.79558

Suresh, P., Long, A.F., Dumont, S., 2020. Microneedle manipulation of the mammalian spindle reveals specialized, short-lived reinforcement near chromosomes. eLife 9, e53807. https://doi.org/10.7554/eLife.53807

Tamura, N., Shaikh, N., Muliaditan, D., Soliman, T.N., McGuinness, J.R., Maniati, E., Moralli, D., Durin, M.-A., Green, C.M., Balkwill, F.R., Wang, J., Curtius, K., McClelland, S.E., 2020. Specific Mechanisms of Chromosomal Instability Indicate Therapeutic Sensitivities in High-Grade Serous Ovarian Carcinoma. Cancer Res 80, 4946–4959. https://doi.org/10.1158/0008-5472.CAN-19-0852

Tovini, L., McClelland, S., 2019. Impaired CENP-E Function Renders Large Chromosomes More Vulnerable to Congression Failure. Biomolecules 9, 44. https://doi.org/10.3390/biom9020044

Truong, M.A., Cané-Gasull, P., de Vries, S.G., Nijenhuis, W., Wardenaar, R., Kapitein, L.C., Foijer, F., Lens, S.M., 2023. A kinesin-based approach for inducing chromosome-specific mis-segregation in human cells. EMBO J 42, e111559. https://doi.org/10.15252/embj.2022111559

Tucker, J.B., Bonema, S.C., García-Varela, R., Denu, R.A., Hu, Y., McGregor, S.M., Burkard, M.E., Weaver, B.A., 2023. Misaligned Chromosomes are a Major Source of Chromosomal Instability in Breast Cancer. Cancer Research Communications 3, 54. https://doi.org/10.1158/2767-9764.CRC-22-0302

Turnham, D.J., Bullock, N., Dass, M.S., Staffurth, J.N., Pearson, H.B., 2020. The PTEN Conundrum: How to Target PTEN-Deficient Prostate Cancer. Cells 9, 2342. https://doi.org/10.3390/cells9112342

Vukušić, K., Tolić, I.M., 2023. CENP-E initiates chromosome congression by opposing Aurora kinases to promote end-on microtubule attachments close to centrosomes. biorxiv. https://doi.org/10.1101/2023.10.19.563150

Vukušić, K., Tolić, I.M., 2022. Polar Chromosomes—Challenges of a Risky Path. Cells 11, 1531. https://doi.org/10.3390/cells11091531

Wandke, C., Barisic, M., Sigl, R., Rauch, V., Wolf, F., Amaro, A.C., Tan, C.H., Pereira, A.J., Kutay, U., Maiato, H., Meraldi, P., Geley, S., 2012. Human chromokinesins promote chromosome congression and spindle microtubule dynamics during mitosis. J Cell

Biol 198, 847–863. https://doi.org/10.1083/jcb.201110060

Waters, J.C., Chen, R.H., Murray, A.W., Salmon, E.D., 1998. Localization of Mad2 to kinetochores depends on microtubule attachment, not tension. J Cell Biol 141, 1181–1191. https://doi.org/10.1083/jcb.141.5.1181

Winters, L., Ban, I., Prelogović, M., Kalinina, I., Pavin, N., Tolić, I.M., 2019. Pivoting of microtubules driven by minus-end-directed motors leads to spindle assembly. BMC Biology 17, 42. https://doi.org/10.1186/s12915-019-0656-2

Woodruff, J.B., Wueseke, O., Hyman, A.A., 2014. Pericentriolar material structure and dynamics. Philos Trans R Soc Lond B Biol Sci 369, 20130459. https://doi.org/10.1098/rstb.2013.0459

Worrall, J.T., Tamura, N., Mazzagatti, A., Shaikh, N., van Lingen, T., Bakker, B., Spierings, D.C.J., Vladimirou, E., Foijer, F., McClelland, S.E., 2018. Non-random Mis-segregation of Human Chromosomes. Cell Rep 23, 3366–3380. https://doi.org/10.1016/j.celrep.2018.05.047

Yajima, J., Edamatsu, M., Watai-Nishii, J., Tokai-Nishizumi, N., Yamamoto, T., Toyoshima, Y.Y., 2003. The human chromokinesin Kid is a plus end-directed microtubule-based motor. EMBO J 22, 1067–1074. https://doi.org/10.1093/emboj/cdg102

Yang, Z., Tulu, U.S., Wadsworth, P., Rieder, C.L., 2007. Kinetochore Dynein Is Required for Chromosome Motion and Congression Independent of the Spindle Checkpoint. Curr Biol 17, 973–980. https://doi.org/10.1016/j.cub.2007.04.056

Yin, Y., Shen, W.H., 2008. PTEN: a new guardian of the genome. Oncogene 27, 5443–5453. https://doi.org/10.1038/onc.2008.241

Zhang, C., Kang, J.S., Asano, S.M., Gao, R., Boyden, E.S., 2020. Expansion Microscopy for Beginners: Visualizing Microtubules in Expanded Cultured HeLa Cells. Current Protocols in Neuroscience 92, e96. https://doi.org/10.1002/cpns.96

Supplementary Material

Supplementary Figures S1-S6

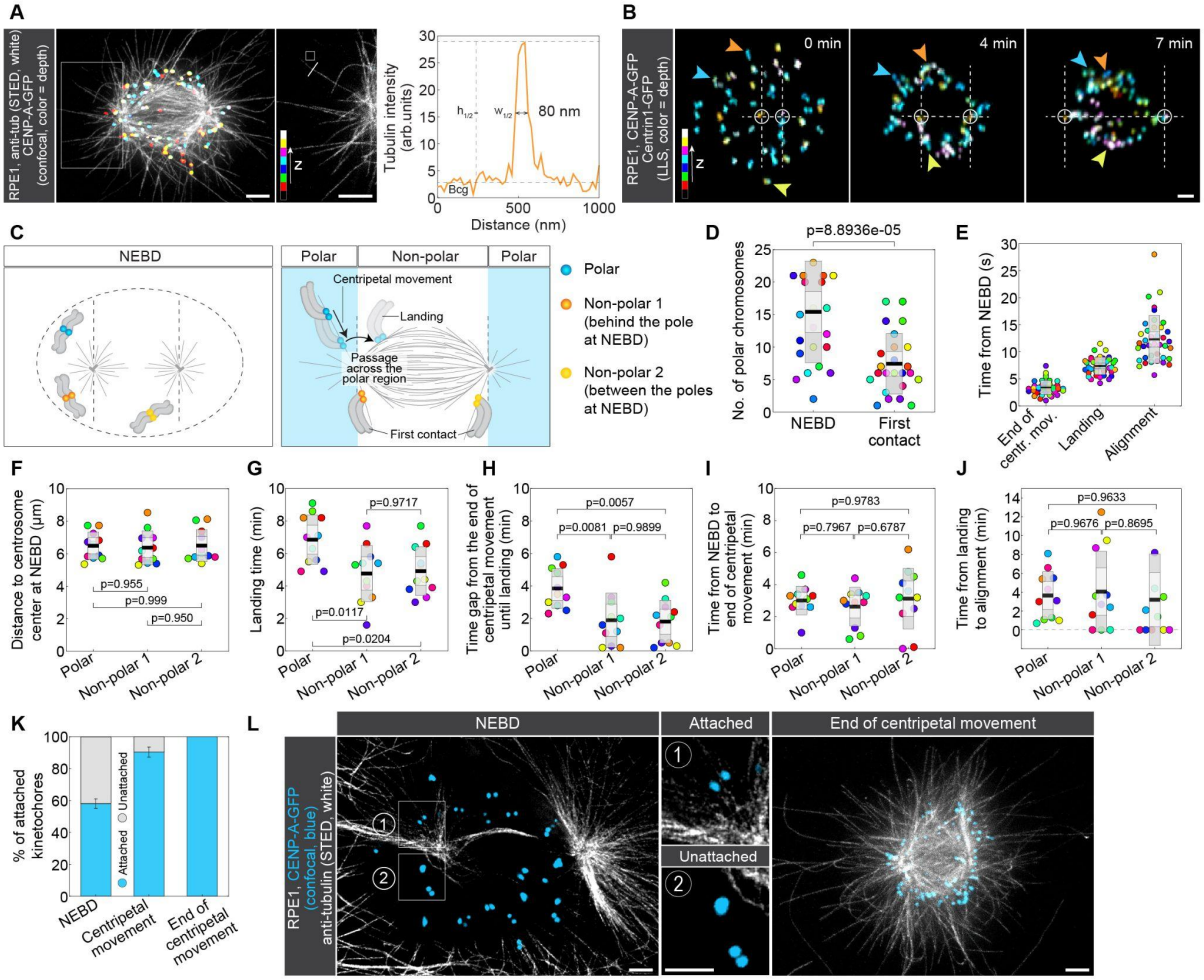

Supplementary Figure 1. **(A)** STED superresolution images of microtubules immunostained for α-tubulin (white) in RPE1 cells stably expressing CENP-A-GFP (colorful, confocal). Images show maximum intensity projection of the whole cell (left) and the inset of a single z-plane with the astral microtubule of interest (right), marked with the white square on the left image. Kinetochores are color-coded for depth with the brgbcmyw LUT in ImageJ throughout 12 z-planes, correspoding to 3.6 µm. Line Tool (length = 1 µm, thickness = 1) and Square Tool (25x25 pixel, corresponding to 0.5x0.5 µm) from ImageJ are drawn on the inset and represent tools to measure the intensity profile of the astral microtubule and the mean intensity of the nearby background, respectively. The graph on the right shows the intensity profile of the line drawn perpendicularly to the astral microtubule in the STED image inset. The resolution is defined as the width of the peak at its half-maximum, after subtracting the background. **(B)** Time-lapse LLS images of RPE1 cells stably expressing CENP-A-GFP and Centrin1-GFP (colorful, lattice light-sheet). Images show maximum intensity projections of 29, 34 and 40 z-planes (4.2-5.8 µm) covering the whole cell, respectively. The blue arrow represents a polar kinetochore, orange and yellow arrows represent non-polar kinetochores located behind the pole or between the poles at NEBD, respectively. All kinetochores are tracked from NEBD

until alignment to the spindle equator. Kinetochores are color-coded for depth with the brgbcmyw LUT in ImageJ. **(C)** Schematic representation of three groups of kinetochores. Blue kinetochores represent polar kinetochores located behind the spindle pole at NEBD and at their first contact with the spindle. Orange kinetochores represent non-polar kinetochores that are located behind the spindle pole at NEBD but between the two poles when they make their first contact with the spindle. Yellow kinetochores represent non-polar kinetochores located between the spindle poles at NEBD and during their first contact with the spindle. Colors for each group correspond to arrows in (B). **(D)** Univariate scatter plot of the number of chromosomes located behind the pole at NEBD and at their first contact with the spindle. Each color represents the same cell at each time point. N = 24 cells from 8 experiments. Statistical analysis: t-test. **(E)** Univariate scatter plot of the time from NEBD until the end of centripetal movement, landing and alignment. Each color represents the same kinetochore pair. N = 39 kinetochore pairs in 20 cells from 8 experiments. **(F-J)** Univariate scatter plot of the (F) distance to centrosome center at NEBD, (G) landing time, (H) time gap from the end of centripetal movement until landing, (I) time from NEBD to centripetal movement, and (J) time from landing to alignment for the three groups of kinetochores described in (C). Each color represents one kinetochore pair. N = 11 kinetochore pairs in 10 cells from 7 experiments. Statistical tests: Anova with post-hoc Tukey test. **(K)** The fractions of kinetochore pairs next to microtubules (blue) and without microtubules in their proximity (gray) during NEBD, centripetal movement and at the end of centripetal movement. N = 241 kinetochore pairs in 15 cells from 6 experiments (NEBD), 73 kinetochore pairs in 4 cells from 3 experiments (centripetal movement), 11 cells from 4 experiments, where all kinetochore pairs located behind the pole had a microtubule attached to them (end of centripetal approaching). **(L)** STED superresolution images of microtubules immunostained for α-tubulin (white) in RPE1 cells stably expressing CENP-A-GFP (blue, confocal) at NEBD and at the end of centripetal movement. Images show a single z-plane at NEBD and a maximum intensity projection of 23 z-planes (6.9 µm) covering the whole cell at the end of centripetal movement. Two types of attachments (attached vs. unattached) are shown in insets from NEBD. **(D-J)** Boxes represent standard deviation (dark gray), 95% confidence interval of the mean (light gray) and mean value (black). **(A,B,L)** Scale bars, 2 µm.

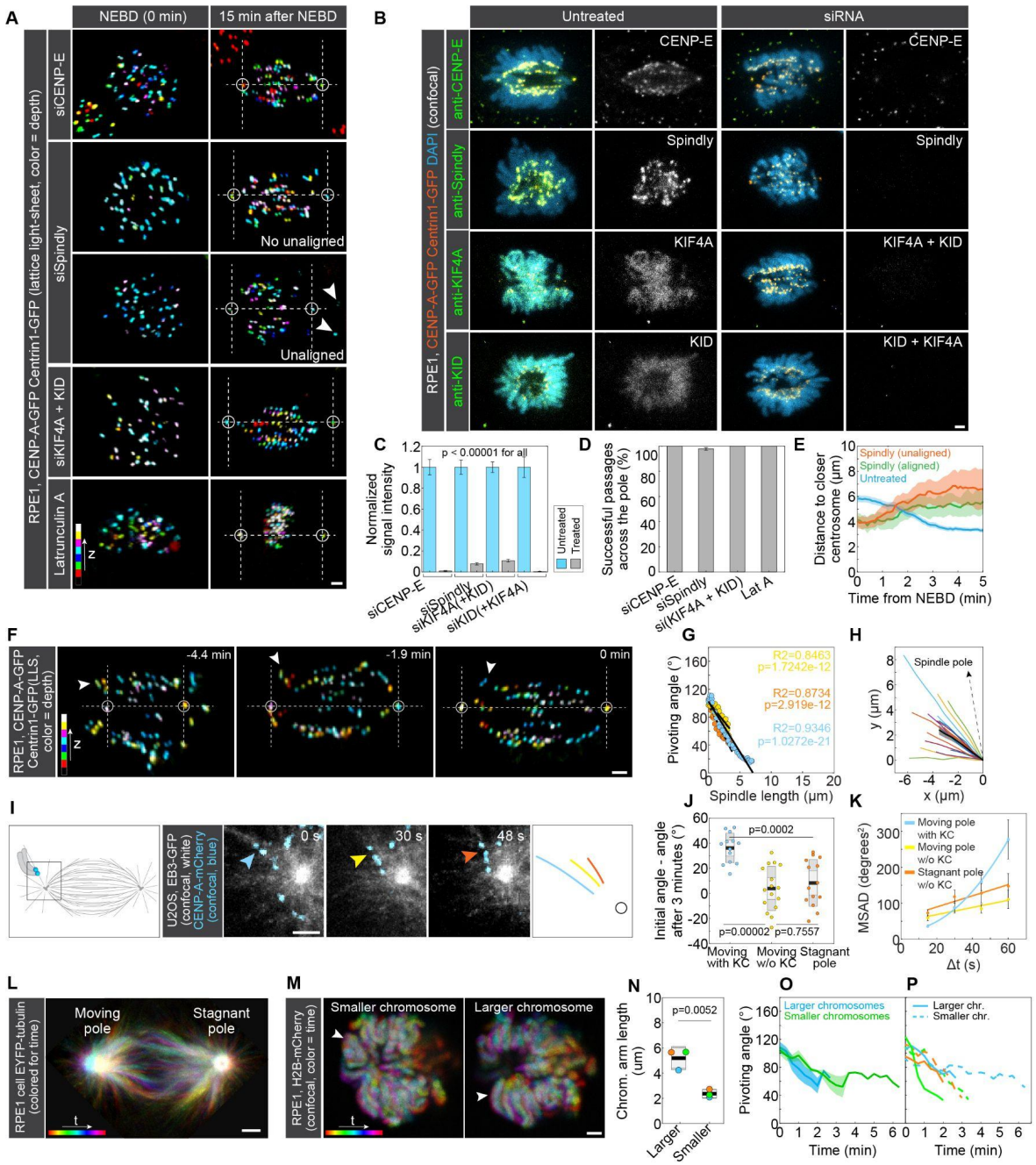

Supplementary Figure 2. (A) Time-lapse images of RPE1 cells stably expressing CENP-A-GFP and Centrin1-GFP (colorful, lattice light-sheet) in CENP-E depletion, Spindly depletion, KIF4A/Kid co-depletion and Latrunculin A treatment. Images show maximum intensity projections of the whole cell. Kinetochores are color-coded for depth with the brgbcmyw LUT in ImageJ throughout 27-77 z-planes, corresponding to 3.9-11.2 µm. White arrows represent unaligned kinetochores after Spindly depletion. **(B)** Fixed untreated, CENP-E, Spindly, and KIF4A/Kid siRNA-treated RPE1 cells stably expressing CENP-A-GFP and Centrin1-GFP (both in orange) and immunostained for CENP-E, Spindly, KIF4A or Kid (each treatment in green). Chromosomes were stained with DAPI (blue) to identify cells in prometaphase. Images are maximum intensity projections of the whole cell (33 z-planes), corresponding to 16.5 µm. **(C)** Normalized signal intensity for treatments in (B) for untreated (blue) and treated (gray) cells. N = 36 control and 36 CENP-E siRNA-treated cells from 3 experiments. N = 32 control and 30 Spindly siRNA-treated cells from 3 experiments. N = 37 control and 35 KIF4A/Kid

siRNA-treated cells from 3 experiments stained with KIF4A antibody. N = 33 control and 30 KIF4A/Kid siRNA-treated cells from 3 experiments stained with Kid antibody. Statistical test: Mann-Whitney U test. **(D)** Fraction of successful passages of polar kinetochore pairs across the spindle pole in cells treated with latrunculin A or in Spindly and CENP-E depletion and KIF4A/Kid codepletion. Successful passage was defined as passage across the 90° mark with respect to the spindle axis within 15 minutes from NEBD. N = all polar kinetochore pairs in 11 cells from 3 experiments for CENP-E. N = 188 polar kinetochore pairs in 12 cells from 6 experiments for Spindly, 4 out of which failed to pass the pole. N = all polar kinetochore pairs in 10 cells from 3 experiments for KIF4A and Kid. N = all polar kinetochore pairs in 10 cells from 4 experiments for Latrunculin A. **(E)** Distance of a polar kinetochore pair to the closer centrosome in time for polar kinetochore pairs in untreated cells (blue), polar kinetochore pairs in Spindly depletion that successfully crossed the pole (green) and polar kinetochore pairs that failed to cross the pole (orange). Values are shown as mean (dark line) and SEM (shaded areas). N = 39 polar kinetochore pairs in 20 untreated cells from 8 experiments. N = 4 polar kinetochore pairs that successfully crossed the pole in 3 Spindly-depleted cells from 2 experiments. N = 4 polar kinetochore pairs that failed to cross the pole in 3 Spindly-depleted cells from 2 experiments. **(F)** Time-lapse images of RPE1 cells stably expressing CENP-A-GFP and Centrin1-GFP (colorful, lattice light-sheet). Images show maximum intensity projections of the whole cell. Kinetochores are color-coded for depth with the brgbcmyw LUT in ImageJ throughout 34-38 z-planes, corresponding to 4.9-5.5 µm. White arrows represent one polar kinetochore tracked from the end of centripetal movement until it passed the spindle pole and landed on the main spindle surface (t = 0 minutes). **(G)** The anticorrelation between the pivoting angle and the spindle length for three individual polar kinetochore pairs as in (F). Linear regression. N = 3 randomly chosen polar kinetochore pairs in 3 cells from 3 experiments. **(H)** The shape of astral microtubules with attached polar kinetochores tracked mid-pivoting. The spindle pole is located in (0,0). N = 16 microtubules in 10 cells from 4 experiments. Values are shown as mean (dark line) and SEM (shaded areas) and individual microtubules are depicted in colors. **(I)** Schematic representation of the imaged region and time-lapse images of U2OS cells stably expressing EB3-GFP (white, confocal) and CENP-A-mCherry (blue, confocal) showing astral microtubule attached to the polar kinetochore pair and pivoting over time (left). Images are temporal maximum intensity projections of a single z-plane in 3-5 sequential time frames during which the comet was visible. Schematic representation of astral microtubules pivoting over time (right). Blue, yellow and orange arrows correspond to the colors of astral microtubules on the scheme to the right. **(J)** Pivoting angle change over a period of 3 minutes from the beginning of pivoting for astral microtubules with polar kinetochores attached to them on the moving pole (blue), microtubules without polar kinetochores attached to them on the moving pole (yellow) and microtubules without polar kinetochores attached to them on the stagnant pole (orange). N = 13 microtubules with polar kinetochores attached to them on the moving pole in 9 cells from 4 experiments. N = 16 microtubules without polar kinetochores attached to them on the moving pole in 10 cells from 4 experiments. N = 14 microtubules without polar kinetochores attached to them on the stagnant pole in 6 cells from 4 experiments. Statistical test: Anova with post-hoc Tukey test. **(K)** Mean squared angular displacement (MSAD) for astral microtubules with polar kinetochores attached to them on the moving pole (blue), microtubules without polar kinetochores attached to them on the moving pole (yellow) and microtubules without polar kinetochores attached to them on the stagnant pole (orange). MSAD = $v^2t^2 + 2D_{MT}\Delta t$ + offset for microtubules with polar kinetochores attached to them on the moving pole and MSAD = $2D_{MT}\Delta t$ + offset for the other two groups of microtubules (Berg, 1993). R2 = 0.999, 0.841 and 0.913, respectively. Error bars represent SEM. N = 16 microtubules with polar kinetochores attached to them on the moving pole in 10 cells from 4 experiments. N = 16 microtubules without polar kinetochores attached to them on

the moving pole in 10 cells from 4 experiments. N = 14 microtubules without polar kinetochores attached to them on the stagnant pole in 6 cells from 4 experiments. **(L)** An image of an RPE1 cell stably expressing EYFP-tubulin (colorful, confocal) and H2B-mRFP (not imaged) with added HaloTag-CENP-A (not shown). The image is a temporal maximum intensity projection of the spindle and centrosome movements over 3 central z-planes (3 µm) and a time period of 4.5 minutes, color-coded for time with the Spectrum LUT in ImageJ. **(M)** Images of RPE1 cells stably expressing EB3-GFP (not shown) and H2B-mCherry (colorful, confocal). Images are temporal maximum intensity projections of a single z-plane showing the smaller chromosome (left) and larger chromosome (right) movements over a time period of 3.3 minutes, color-coded for time with the Spectrum LUT in ImageJ, and corresponding to images in Figure 2C. Chromosomes of interest are marked with white arrows. **(N)** Chromosome arm length for larger and smaller chromosomes. Each color represents one pairing of a larger and a smaller chromosome within the same cell. N = 3 chromosomes in 3 cells from 2 experiments each. Statistical test: t-test. **(O)** The pivoting angle in time for smaller (green) and larger (blue) chromosomes in time. Values are shown as mean (dark line) and SEM (shaded areas). **(P)** The pivoting angle for individual smaller (dashed line) and larger (full line) chromosomes in time. Each color represents one pairing of a larger and a smaller chromosome in one cell. **(J,N)** Boxes represent standard deviation (dark gray), 95% confidence interval of the mean (light gray) and mean value (black). **(A,B,F,I,L,M)** Scale bars, 2 µm.

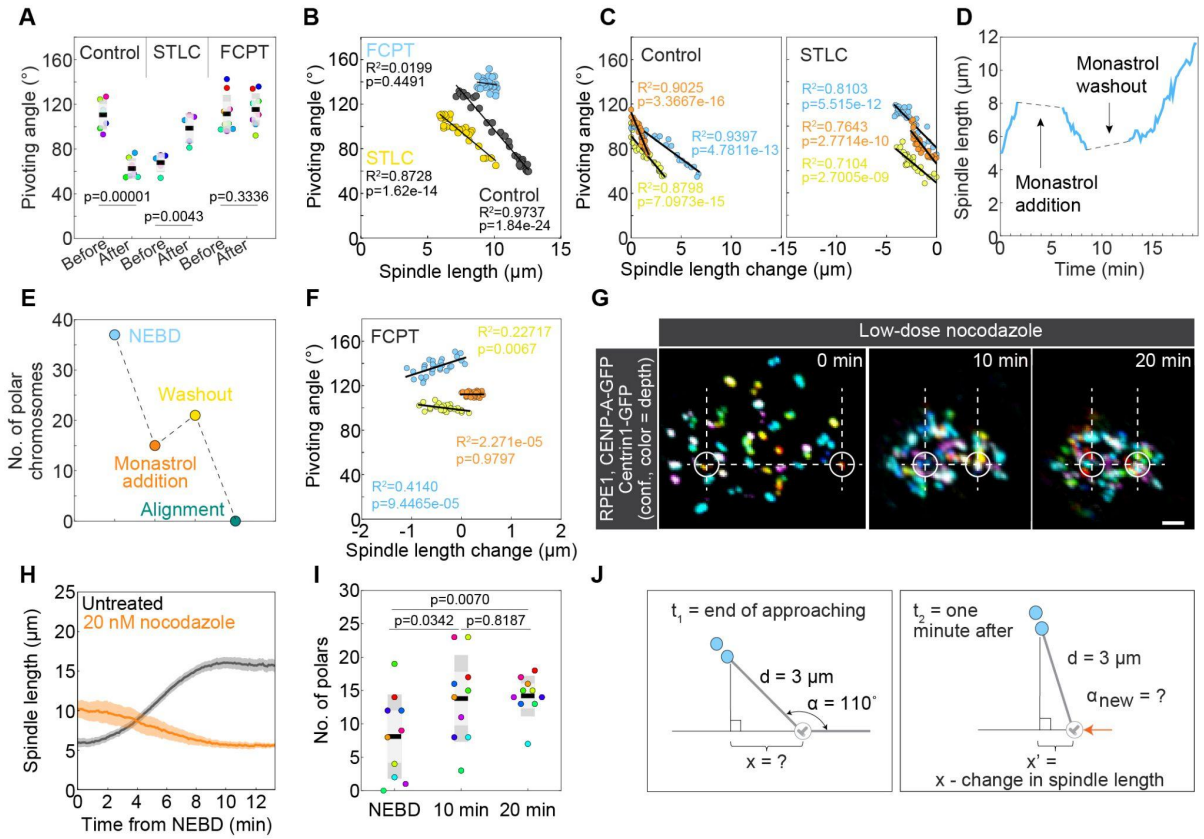

Supplementary Figure 3. (A) Univariate scatter plot of the pivoting angle before and 5 minutes after the addition of DMSO (left), STLC (middle) and FCPT (right). Each color represents a different kinetochore pair. If landing occurred less than 5 minutes after the addition of DMSO, it was taken as the final step instead. N = 7 kinetochore pairs in 7 cells from 7 experiments (DMSO), 5 kinetochore pairs in 3 cells from 3 experiments (STLC), 9 kinetochore pairs in 7 cells from 7 experiments (FCPT). Statistical test: paired t-test. **(B)** Anticorrelation of the pivoting angle and spindle length for the control, STLC and FCPT treatment. N = 1 kinetochore pair from 1 cell and 1 experiments for each. **(C)** Anticorrelations of the pivoting angle and spindle length change for another three individual kinetochore pairs in control (left) and STLC treatment. N = 3 kinetochore pairs in 3 cells from 3 experiments. **(D)** Change of spindle length in time during the monastrol washout experiment. Dashed lines denote the time required for the addition or washout of the inhibitor together with the time required for the spindle length to start changing. N = 1 kinetochore pair in 1 cell from 1 experiment. **(E)** Number of chromosomes behind the pole at nuclear envelope breakdown (NEBD, blue), just before monastrol addition (orange), just before monastrol washout (yellow) and in late prometaphase following monastrol washout (dark green). N = all chromosomes located behind the pole at any given moment in 1 cell from 1 experiment. **(F)** Anticorrelation of the pivoting angle and spindle length change for another three individual kinetochores in FCPT treatment. N = 3 kinetochore pairs in 3 cells from 3 experiments. **(G)** Time-lapse lattice light-sheet images of RPE1 cells stably expressing CENP-A-GFP and Centrin1-GFP (colorful, confocal) in low-dose nocodazole treatment (20 nM). Images are maximum intensity projections of the whole cell. Kinetochores are color-coded for depth with the brgbcmyw LUT in ImageJ throughout 37-52 z-planes, corresponding to 5.4-7.5 µm. White circles represent spindle poles, dashed lines represent the long spindle axis and lines perpendicular to it denote the borders of the polar region. **(H)** Change of spindle length in time from NEBD for untreated (gray) and cells treated with 20 nM nocodazole (orange). Values are shown as mean (dark line) and SEM (shaded

areas). N = 20 untreated cells from 8 experiments. N = 10 nocodazole-treated cells from 4 experiments. **(I)** The number of chromosomes behind the pole at NEBD and 10 and 20 minutes after NEBD for cells treated with 20 nM nocodazole. Each color represents one cell. N = 10 cells from 4 experiments. Statistical test: repeated measures Anova. **(J)** Schematic representation for calculating the theoretical line shown in Figure 3H. d = distance between the closer spindle pole and the kinetochore pair, x = distance between the spindle pole and the orthogonal projection of the kinetochore pair onto the spindle axis, x' = x – change in spindle length, α = pivoting angle, α_{new} = calculated as the arccos (x'/d). The values of d and α were obtained from the DMSO and STLC experiments. **(A,I)** Boxes represent the standard deviation (dark gray), 95% confidence interval of the mean (light gray) and mean value (black). **(B,C,F)** Linear regression. **(G)** Scale bar, 2 µm.

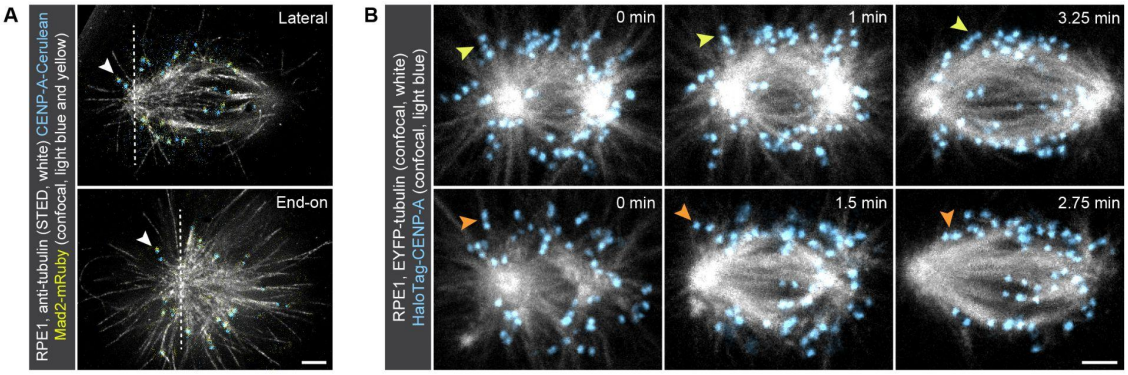

Supplementary Figure 4. **(A)** STED superresolution images of microtubules immunostained for α-tubulin (white) in RPE1 cells stably expressing CENP-A-Cerulean (blue) and Mad2-mRuby (yellow). Images show single z-planes of spindles with laterally or end-on attached polar kinetochores shown in Figure 4. **(B)** Time-lapse confocal images of RPE1 cells stably expressing EYFP-α-tubulin (white) and H2B-mRFP (not imaged) with added HaloTag-CENP-A (blue). The first row represents a kinetochore pair that constantly remains attached to the same microtubule during pivoting. The second row represents a kinetochore pair that changes the attachment of its further kinetochore during pivoting from lateral to bilateral. The images are maximum intensity projections of 3 central z-planes spanning 3 µm. Kinetochores are smoothed with 0.75-mm-sigma Gaussian blur. **(A-B)** Scale bars, 2 µm.

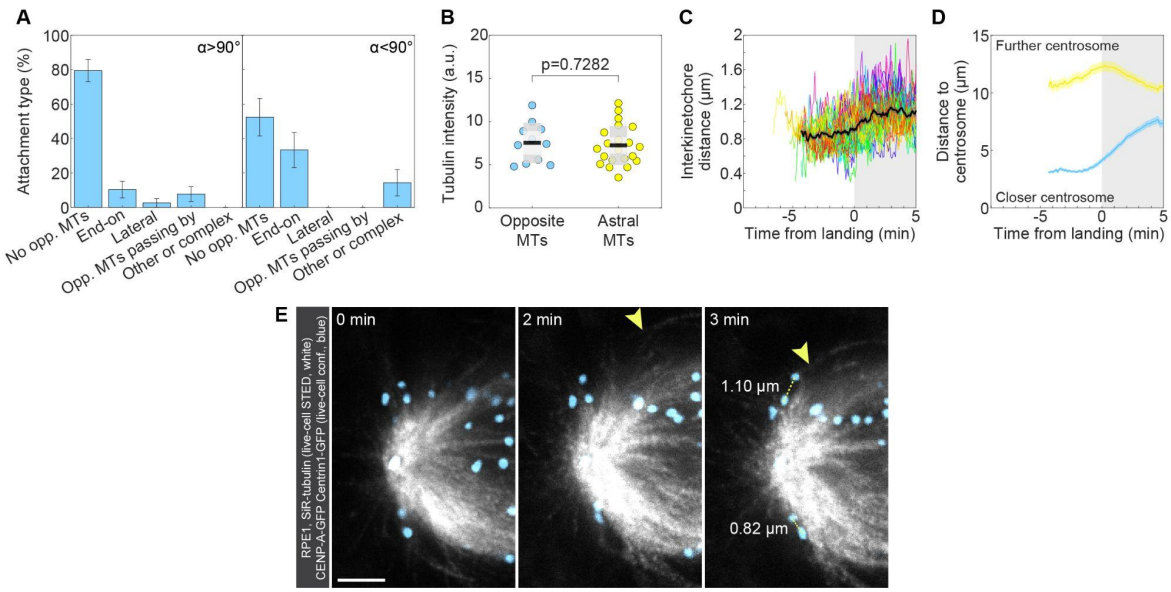

Supplementary Figure 5. (A) Percentage of different attachment types with microtubules from the opposite side of the spindle for kinetochores between the end of centripetal movement and landing as measured from STED images in the areas with the pivoting angle above or below 90°. N = 8 kinetochore pairs in 8 cells from 3 experiments for above 90°. N = 10 kinetochore pairs in 9 cells from 4 experiments for below 90°. **(B)** Univariate scatter plot of the tubulin intensity for microtubules that come from the opposite side of the spindle and attach to polar kinetochores (blue) and astral microtubules (yellow). Boxes represent the standard deviation (dark gray), 95% confidence interval of the mean (light gray), and mean value (black). N = 11 opposite microtubules in 10 cells from 4 experiments. N = 22 astral microtubules in the same 10 cells from 4 experiments. Statistical test: t-test. **(C)** Interkinetochore distance of polar kinetochores over time from the end of centripetal movement. Different colors correspond to different kinetochore pairs. N = 39 kinetochore pairs in 20 cells from 8 experiments. **(D)** Distance to further (yellow) and closer (blue) centrosome over time for polar kinetochores from the end of centripetal movement. Values are shown as mean (dark line) and SEM (shaded areas). N = 39 kinetochore pairs in 20 cells from 8 experiments. **(E)** Time-lapse live-cell STED images of RPE1 cells stably expressing CENP-A-GFP and Centrin1-GFP (blue, confocal) and stained with 100 nM SiR-tubulin (STED, white). Each image represents a single z-plane. The yellow arrow denotes the microtubule coming from the opposite side of the spindle. Dashed yellow lines represent the interkinetochore distance at landing. **(E)** Scale bar, 2 µm.

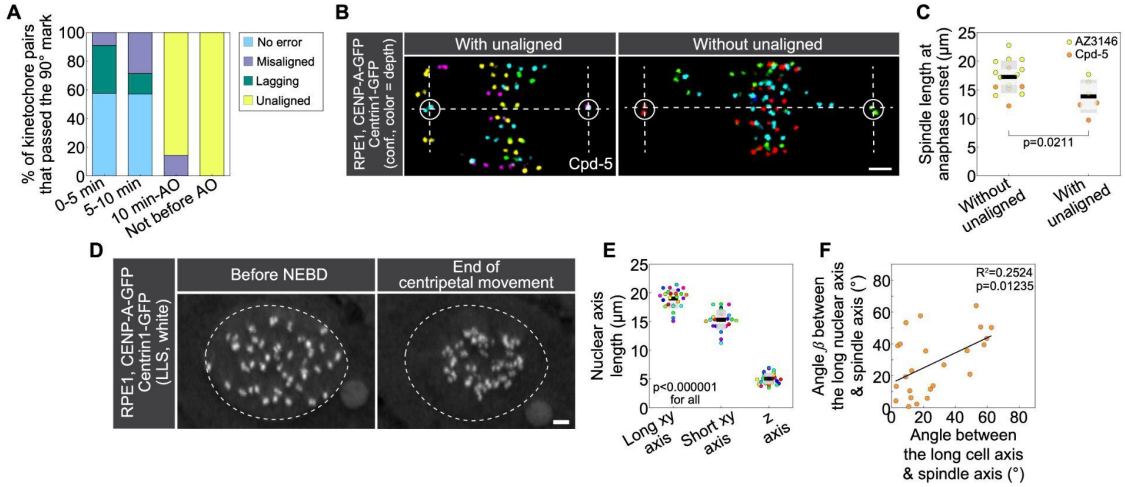

Supplementary Figure 6. (A) Fractions of kinetochore pairs that passed the 90° mark in the first five minutes after NEBD, between 5 to 10 minutes after NEBD, between 10 minutes after NEBD and the anaphase onset, and those that failed to pass the 90° mark before anaphase onset. Kinetochore pairs are classified as no error (blue), lagging (green), misaligned (purple) and unaligned (yellow). N = 52 kinetochore pairs initially located behind the pole in 7 cells from 4 experiments. **(B)** Still images of RPE1 cells stably expressing CENP-A-GFP and Centrin1-GFP (colorful, confocal) and treated with Mps1 inhibitor Cpd-5. Images show maximum intensity projections of the imaged cells. The left panel represents cells with unaligned chromosomes and the right panel represents cells without unaligned chromosomes at anaphase onset. Circles depict the spindle poles and dashed lines the boundaries of the polar region. Kinetochores are color-coded for depth with the Spectrum LUT in ImageJ throughout 4 z-planes, corresponding to 4 µm. Cells were originally imaged as part of the dataset for Klaasen et al., 2022. **(C)** Univariate scatter plot of the spindle length at anaphase onset for cells without (left) and with (right) unaligned chromosomes at anaphase onset. Cells are divided based on the treatment, to those treated with AZ3146 (yellow) or Cpd-5 (orange). N = 7 cells from 4 experiments for AZ3146. N = 15 cells from 4 experiments for Cpd-5. Statistical test: t-test. Cells with added Cpd-5 were originally imaged as part of the dataset for Klaasen et al., 2022. **(D)** Time-lapse images of RPE1 cells stably expressing CENP-A-GFP and Centrin1-GFP (white, lattice-lightsheet). Images show maximum intensity projections of 36 and 42 z-planes covering the whole cell, corresponding to 5.2 µm and 6.1 µm, respectively. The left image represents the nucleus before NEBD and the right image represents the kinetochore and centrosome arrangement at the end of centripetal movement. Dashed lines denote the borders of the nucleus as outlined before NEBD. **(E)** Univariate scatter plot of the long xy nuclear axis length (left), short xy nuclear axis length (middle) and z nuclear axis length (right). N = 24 cells from 8 experiments. Statistical test: Anova with post-hoc Tukey test. **(F)** A correlation between the angle that the long nuclear axis in interphase forms with the spindle axis at the end of the centripetal movement (Angle - nucleus) and the angle that the long cellular axis in interphase forms with the spindle axis at the end of the centripetal movement. N = 24 cells from 8 experiments. Linear regression. **(C,E)** Boxes represent standard deviation (dark gray), 95% confidence interval of the mean (light gray) and mean value (black). **(B,D)** Scale bar, 2 µm.

A

Cell lines with detected misalignment issues	Chromosomes behind the pole	Short spindles	Chromokinesin status	Citations	
Ovarian cancer					retrieved by using cBioportal (Cerami et al., 2012; Gao et al., 2013, de Burijn et al., 2023, Barretina et al., 2012, Ghandi et al., 2019, Reinhold et al., 2012)
OVSAHO	Yes	Yes	No known alterations	Tamura et al., 2020 Risteski et al., 2024 (unpublished data from Tolić lab)	
OVKATE	No	Yes	No known alterations		
Cov318	N/A	N/A	No known alterations		
Breast cancer					
MCF7	N/A	N/A	KIF4A - homodeletion KID - splice mutation (unknown significance)	Tucker et al., 2023	
T47D	N/A	N/A	No known alterations		
Cal51	N/A	N/A	No known alterations		
Cervical cancer					
HeLa	N/A	No	No known alterations	Gomes et al., 2022 Kletter et al., 2022	
Bone cancer					
U2OS	Yes	No	KIF4A - amplification	Gomes et al., 2022 Klaasen et al., 2022 Bird and Hyman, 2008	

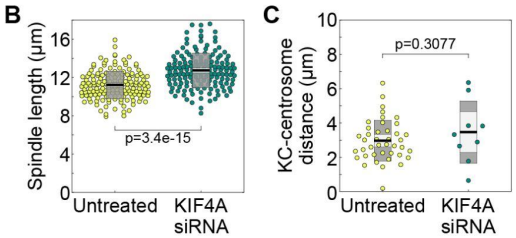

Supplementary Figure 7. (A) Screen of cancer cell lines for studying elongation-driven pivoting. Criteria included misalignment issues with chromosomes behind the pole in metaphase, short spindles and no alterations in chromokinesins. **(B)** Univariate scatter plot of the spindle length in untreated (yellow) and KIF4A siRNA treated (green) OVSAHO cells. Measurements were done on fixed metaphase spindles as in Figure 7A. N = 160 untreated cells from 3 experiments. N = 157 KIF4A siRNA-treated cells from 3 experiments. Statistical test: t-test. (C) Univariate scatter plot of the distance between the closer centrosome and the kinetochores of unaligned chromosomes for untreated (yellow) and KIF4A siRNA treated (green) OVSAHO cells. Measurements are done on fixed metaphase spindles as in Figure 7A. N = 39 chromosomes in 25 untreated cells from 3 experiments. N = 7 chromosomes in 6 KIF4A siRNA-treated cells from 2 experiments. Statistical test: t-test. **(B, C)** Boxes represent standard deviation (dark gray), 95% confidence interval of the mean (light gray) and mean value (black).